The structure of turbulent flames in fractal- and regular-grid-generated turbulence

T Sponfeldner[1], N Soulopoulos[1], F Beyrau[1], Y Hardalupas[1], AMKP Taylor[1,*] and JC Vassilicos[2]

[1]*Department of Mechanical Engineering, Imperial College London, London, SW7 2AZ, United Kingdom*

[2]*Department of Aeronautics, Imperial College London, London, SW7 2AZ, United Kingdom*

[*]*Corresponding author: a.m.taylor@imperial.ac.uk*

Abstract

This study reports on the use of fractal grids as a new type of turbulence generators in premixed combustion applications. Fractal grids produce turbulence fields which differ from those formed by regular turbulence generators such as perforated plates or meshes. Fractal grids generate high turbulence intensities over an extended region some distance downstream of the grid with a comparatively small pressure drop. Additionally, the integral scale of the flow does not change downstream of the grid. The extended region of high turbulence can also be optimized for the specific application at hand by changing certain parameters of the grid which makes it possible to design the downstream development of the turbulence field. Four space-filling fractal square grids were designed to independently vary the resulting turbulent field and a regular square mesh grid with similar turbulent intensity acted as a reference case. The structure of the resulting premixed V-shaped flames was investigated using Conditioned Particle Image Velocimetry (CPIV). At the same downstream position, flames in the turbulence field of fractal grids showed larger turbulent burning velocity compared to flames in regular grid generated turbulence. However, when compared for the same turbulence intensity, flames in fractal grid generated turbulence produced similar turbulent burning velocities

compared to flames in regular grid generated turbulence. In particular, it could be shown that theories such as Taylor's theory of turbulent diffusivity and Damköhler's theory of premixed flame propagation, which were deduced from regular turbulence fields, adequately described the increase of effective flame surface area due to the increase in turbulence intensity. Using fractal grids allows the independent variation of the turbulent fluctuations, the integral length scale and the turbulent Reynolds number. An unexpected finding was that the burning velocity ratio, S_t/S_l was negligible influenced by the integral length scale. A correlation between the burning velocity ratio, s_t/s_l, and the normalized velocity fluctuations of the flow, u'/s_l, showed a negligible influence of the integral scale on the turbulent burning velocity. A literature review revealed that the influence of the integral scale on the turbulent burning velocity is still unclear and further research is required. In this context, fractal grids are particularly helpful as they cover a wider range of integral length scales for sufficiently turbulent flows, $u' \geq s_l$, compared to regular grids.

Keywords

turbulent premixed flames, turbulent burning velocity, fractal grids, multi-scale grids, turbulence-flame interaction, Conditioned Particle Image Velocimetry

1 Introduction

Turbulent premixed flames are of great importance for technical combustion systems as these can produce high power densities and low pollutant emissions at the same time. The impact of turbulent flow field characteristics on the flame is of importance in technical applications because it greatly increases the apparent propagation speed – the so-called "turbulent burning velocity" and knowledge of the dependence of the magnitude of the turbulent burning velocity on the turbulence is valuable and interesting. For basic research into the dependence of the characteristics of the turbulence, it is convenient to use turbulence generating grids such as perforated plates or meshes. These grids are usually

placed at distances of several characteristic mesh sizes upstream of the flame to ensure a well-developed velocity field. Although such grids can generate high levels of turbulence near the grid, the turbulence decays quickly with downstream distance [1], and, as a consequence, the resulting flames are exposed to rather low turbulence intensities.

Correlations for the dependence of the turbulent burning velocity on the turbulent characteristics of the flow field have long been produced and mostly incorporate a dependence on the flow integral length scale. In an experiment, the mean velocity is typically changed in order to produce larger turbulent fluctuations; however, it has been shown, for example, that allowing a simultaneous change of the mean velocity and the turbulent characteristics can produce misleading correlations, [2]. Consequently, the ability to independently vary the turbulent quantities it is of great importance. To achieve this, we utilize fractal grids in premixed turbulent combustion experiments.

Vassilicos *et al.* [3-6] proposed fractal grids as a new type of low blockage turbulence generators with a number of potential applications [7-14]. Fractal grids consist of structures with multiple length scales rather than one length scale. Extensive wind tunnel measurements have shown that fractal grids generate a long region of downstream evolution of turbulence which is fundamentally different from Richardson-Kolmogorov cascading turbulence [15]. The turbulence intensity initially builds up in a distinct production region until it reaches its maximum value and then decays further downstream at a rate that is different to that of regular turbulence grids. Moreover, during the decay of turbulence the integral length scale of the flow remains almost constant whereas the integral scale in regular turbulence fields usually increases with downstream distance. The downstream position of the maximum turbulence intensity is determined by the blockage ratio (the ratio between the area occupied by the grid and the enclosing duct area) and the ratio between the sizes of the largest and the smallest structures of the fractal grid [3]. It

has also been shown that when both grids have the same blockage ratio, fractal grids can produce more than 30% higher turbulence intensities than regular grids [5]. These characteristics might have potential for technical combustion applications because larger flame surfaces per unit volume (*i.e.* power densities) can be achieved due to the higher turbulence intensity. Moreover, the increase in turbulence intensity with increasing distance from the grid seems attractive because this implies larger turbulent flame speeds at some distance from the grid than with a regular grid.

Recently, it has been shown by Mazellier *et al.* [16] that flow fields with similar turbulence characteristics to those of the mentioned fractal grids can be generated using an arrangement of multiple perforated plates with blockage ratios of 50% to 70%. These so-called multi-scale injectors produce turbulence levels comparable to fractal grids, albeit at a much greater pressure drops.

In this work we use fractal grids designed in a similar way to those in [3] as low blockage ($\sigma \approx 35\%$) turbulence generators in a premixed combustion application to study the effect of fractal grid generated turbulence on the structure of premixed flames and to validate existing, semi-empirical correlations of turbulent burning velocity. With these grids, and current manufacturing limitations, turbulence intensities of around 15% can be achieved at distances of 15 to 20 characteristic lengths from the grids. The fact that the velocity fluctuations generated by fractal grids increase over a long downstream distance is particularly interesting in premixed combustion as this makes it possible to achieve the highest turbulence intensity well downstream of the grid, at the location of the flame. As the downstream position of the maximum turbulence intensity can be changed by varying the design parameters of the grid, fractal grids could also be used to tailor the turbulence field in the region of the flame, according to the requirements of the particular combustion application. A recent comparison [14] of flames in fractal and regular grid generated

turbulence has shown that for the same downstream position fractal grids produce flames with more wrinkling, a higher flame surface density and higher turbulent burning velocities.

The turbulent burning velocity, s_t, is often an important quantity in premixed combustion when it comes to assessing the burning rate at which unburnt gases are consumed by the flame. Based on numerous experimental investigations some obvious qualitative trends of the turbulent burning velocity in the region of moderate turbulence are well-known: the increase of s_t with increasing root-mean-squared velocity fluctuations of the flow, u', and the increase of s_t with increasing laminar burning velocity, s_l. Notably, Damköhler [17] was one of the earliest to provide a theoretical explanation for the increase of a flame's burning rate in the presence of a turbulent flow field. He deduced the well-known relation whereby the increase in turbulent burning velocity can be associated with the increase in effective flame surface area, $s_t/s_l \propto A_t/A_l$. He suggested that for large-scale turbulence (now called the corrugated flamelet regime) the interaction between flow field and flame front is purely kinematic and that the turbulent burning velocity should therefore depend only on the root-mean-squared velocity fluctuations of the flow, $s_t \propto u'$. For small-scale turbulence (now identified with the thin reaction zone regime) he suggested that rate of transport between the unburnt gases and the reaction zone of the flame is increased. Thus, the turbulent burning velocity should not only depend on the velocity ratio, u'/s_l, but also on the turbulence length scale of the flow, L. Damköhler proposed to use the relation $s_t/s_l \propto (D_t/D_l)^{1/2} = (u'L/s_l\delta_l)^{1/2}$, where $D_t = u'L$ and $D_l = s_l\delta_l$ are the turbulent and laminar diffusivity of the flow, respectively, δ_l is the thermal flame thickness and L is the integral length scale of the flow.

Over the last decades a number of investigations were dedicated to investigate the effect of turbulence on the turbulent burning velocity. Articles by Bray [18], Bradley [19] and Abdel-Gayed [20] reviewed the experimental data that was available to them and discussed the many physical parameters that affect the burning rate of a flame, such as the Karlovitz [21], Markstein [22], Zeldovich [21] or Lewis numbers [23]. In aiming towards a fundamental theoretical description of the turbulent burning velocity many authors during the 80's and 90's noticed the self-similar appearance of the flame surface [24] and proposed that Damköhler's flame surface area ratio may be expressed in terms of an outer and inner length scale of the flow, $A_t/A_l \propto (\varepsilon_o/\varepsilon_i)^{D_f-2}$, with D_f as the fractal dimension [25] (note that this "fractal dimension" is not related to the existence of a fractal grid). By choosing the integral scale L as the outer cut-off frequency and the inner cut-off frequency as either the Kolmogorov scale η [26] or the Gibbson scale λ_G [27], a large number of correlations of the turbulent burning velocity [18, 21, 24, 28] evolved as a function of two dimensionless quantities: the turbulent Reynolds number, $\mathrm{Re}_t = u'L/\nu$, and the velocity ratio u'/s_l. One prominent result of this theoretical approach is the correlation by Gülder [28], $s_t/s_l = 1 + 0.62\,\mathrm{Re}_t^{1/4}(u'/s_l)^{1/2}$. Although Gülder [29] later concluded that fractal theory is not suitable for a description of the turbulent burning velocity, which is widely accepted today, the turbulent Reynolds number and the velocity ratio, u'/s_l, nowadays still remain two of the most important dimensionless quantities used for the prediction of the turbulent burning velocity. Often the equation, $s_t/s_l = 1 + C(u'/s_l)^n$, is used for empirical correlations of the turbulent burning velocity, where n is an adjustable parameter with a value close to 0.5 [22, 30] and C depends either on the length scale ratio, L/δ_l, as originally proposed by Damköhler [17] and theoretically argued by Peters [31], or C is expected to be proportional to the turbulent Reynolds number, $C \propto u'L/\nu$. The current

FLUENT code, for example, uses the empirical correlation $s_t/s_l = 1 + A(u'L/\nu)^{1/4}(u'/s_l)^{1/2}$ based on ref. [32].

In this paper we investigate the effect of fractal grid generated turbulence on the structure of premixed flames, evaluate the validity of existing semi-empirical correlations of turbulent burning velocity as applied to flames subjected to turbulence derived from fractal grids and assess the potential benefits of using fractal grids as turbulence generators in premixed combustion applications. The paper is organized as follows. First, the structure of the fractal square grid is explained and the grids investigated in this study are presented. Then the experimental setup together with a brief description of the measurement techniques is given. The non-reacting flow fields of fractal grids are characterized and differences to regular grid generated turbulence are highlighted. The homogeneity and isotropy of the non-reacting flow fields were compared in the region where the flame would be established as this is crucial for the assessment of the flames. Finally, flames which have been stabilized in the turbulent flow fields of the two types of grids are compared in terms of the mean flame surface density, the flame brush thickness, the flame front curvature and the turbulent burning velocity. The measured burning velocity ratios, s_t/s_l, are then correlated with the normalized velocity fluctuations of the flow, u'/s_l, and the obtained correlation is critically discussed. The paper ends with conclusions drawn from the experimental comparison and presents ways on how current correlations of turbulent burning velocity could potentially be improved.

2 Investigated Grids

The fractal grids used in this study consisted of a planar square pattern which was repeated at different length scales across the grid. At successive iterations, where the scale of the square decreased, the number of squares was increased by a factor of four. Each length scale iteration j is defined by the bar-width d_j and the bar-length l_j that form the

square and is related to the iteration *j-1* by $d_j = R_d\, d_{j-1}$ and $l_j = R_l\, l_{j-1}$, with R_d and R_l the bar-width and bar-length ratio, respectively. According to Hurst *et al.* [3] a space-filling geometry is achieved when the fractal dimension of the grid, $D_f = \log 4/\log(1/R_l)$, approaches its maximum value of 2, *i.e.* R_l = 0.5. A schematic of the fractal geometry is shown in Fig. 1, along with the dimensions of the 0th and j^{th} iteration. The blockage ratio of the grid, which was one of the parameters varied in this study, can be derived from the geometrical dimensions of the grid and is defined as the ratio between the area covered by the grid *A* and the duct's cross sectional area T^2 using,

$$\sigma = \frac{A}{T^2} = \frac{l_0 d_0 \sum_{j=0}^{N-1} 4^{j+1} 0.5^j R_d{}^j}{T^2} - \frac{d_0{}^2 \sum_{j=1}^{N-1} 2^{2j+1} R_d{}^{2j-1} + d_0{}^2 \sum_{j=0}^{N-1} 2^{2j+2} R_d{}^{2j}}{T^2}. \quad (1)$$

Here, l_0 and d_0 denote the length and the width of the largest bar, respectively. *N-1* denotes the overall number of iterations. Other references such as [3] or [4] use slightly different approximations of Eq. 1 for calculating the blockage ratio and vary in the degree of accuracy obtained.

In this study four different fractal square grids (FGs) were designed. All grids were designed in order to fit into a rectangular duct of width *T*, *i.e.* $T = \sum_{j=0}^{N-1} l_j - \sum_{j=0}^{N-2} d_j$. The grids varied either in the blockage ratio, σ, the bar-width ratio, R_d, or the number of fractal iterations, *N*, while the other two parameters were kept constant. A regular square grid with a blockage ratio of 60% and a mesh size of *M* = 7.75 mm was also designed for comparison. The investigated grids are shown in Fig. 2 and more detailed information about the design parameters of the grids can be found in Table 1. All grids were made of stainless steel and had a thickness of 1.5 mm.

An important element of the grid design was that the velocity fluctuations, the integral length scale and the turbulent Reynolds number were independently varied in the same experimental setup. This is in contrast to the more common experimental situation

where changing the mean velocity results in changes of the turbulent flow field characteristics as well.

3 Experimental Setup and Measurement Techniques

3.1 Burner

The effect of fractal grid generated turbulence on the structure of premixed flames was investigated in turbulent V-shaped flames of methane and air, stabilized on a cylindrical rod of 1mm diameter, downstream of the burner exit. The burner consisted of a rectangular duct of width $T = 62$ mm upstream of the turbulence grid and four interchangeable downstream ducts of various lengths. This allowed measurements to be obtained at different downstream positions from the grid with similar distance between the flame holding wire and the burner exit. The upstream duct was 500 mm long and the four downstream ducts had a length of 30 mm, 100 mm, 150 mm and 200 mm. A schematic of the burner as well as the coordinate system, which is referenced to the position of the grid, is given in Fig. 3. A mixture of methane and air entered the burner through four 4 mm diameter nozzles at the bottom of the burner. A perforated plate of 1 mm holes and three layers of glass beads of 10 mm diameter were used to break up large structures of the flow. Inside the upstream duct, 350 mm downstream of the burner inlet, a conditioning section was located which consisted of a perforated plate with 1 mm holes and a 50 mm long honeycomb structure to generate a spatially homogenous velocity profile across the majority of the burner exit. The whole burner was mounted on a frame allowing for height adjustments and precise vertical alignment. The bulk flow velocity was adjusted with mass flow controllers and set to 4 m/s for the non-reacting and the reacting cases, resulting in a flow Reynolds number of 16,000 based on the characteristic width of the duct of 62 mm and cold flow physical properties. The free stream turbulence of the burner without any turbulence grid in place was measured to be 3%.

Premixed flames with three different equivalence ratios of $\phi = 0.7$, 0.8 and 0.9 were investigated. The flames were stabilized on a 1mm diameter wire across the burner exit. In a first set of measurements, the wire was positioned 30 mm downstream of the 150 mm long duct. This set of measurements is referred to as FG1 to FG4 (fractal grids 1-4) and RG-180 (the regular grid with the wire positioned 180 mm downstream of the grid). In a second set of measurements the wire was positioned 20 mm downstream of the 30 mm long duct. At 50 mm downstream of the regular grid the turbulence intensity, $u'/\bar{u}$, produced by the RG was around 14% which is a similar level of turbulence intensity compared to those produced by the FGs at 180 mm, as will be shown later. The second set of measurements is referred to as RG-50.

3.2 Hot-wire

The downstream characterisation of the isothermal turbulence fields was performed with a one-component hot-wire anemometer operated in constant temperature mode (CTA). Signal conditioning and analogue-to-digital conversion were done by a DANTEC Streamline CTA module. Square-wave testing of the balancing bridge revealed a cut-off frequency of 22 kHz at the standard -3dB limit. All measurements were performed with a 55P11 DANTEC miniature probe and a 5 μm diameter platinum-plated tungsten wire with a sensing length of 1.25 mm. The voltage output of the probe was calibrated before and after each run with the built-in DANTEC calibration unit using a fourth-order polynomial fit. The ambient temperature was monitored during the measurements in order to compensate for a temperature drift and the probe was mounted on a three axis precision translation stage for accurate positioning. Measurements along the centreline of the burner (*z*-axis) were obtained from 50 mm to 300 mm at 10 mm intervals using the 100 mm, 150 mm and 200 mm downstream ducts, without the presence of rod used for flame stabilisation for the reacting experiments. The analogue signal was

low-pass filtered in order to avoid aliasing of higher frequencies and then sampled by a 16-bit National Instruments card (PCI-6013) at a sampling frequency of 20 kHz, which was about 5 times the estimated Kolmogorov frequency $f_\eta = \bar{u}/(2\pi\eta)$. The total duration of each run was 2 min, corresponding to approximately 50,000 integral time scales, which was long enough to obtain converged statistics of the flow fields. The statistical uncertainty for the mean and variance of the velocity is less than 0.1%, calculated using their sampling distributions.

From the velocity signal the temporal autocorrelation of the streamwise velocity fluctuations $g(\tau) = \overline{\left(u(t) - \overline{u(t)}\right)\left(u(t+\tau) - \overline{u(t+\tau)}\right)}/\overline{u(t)^2}$ was calculated for temporal separations τ. The integral time scale of the flow was calculated by integrating $g(\tau)$ up to the first zero crossing t_0 of the autocorrelation function [33],

$$T = \int_0^{t_0} g(\tau) d\tau \,. \tag{2}$$

It was checked that the first zero crossing was at least 5 times the integral time scale in order to take into account the full decay of the autocorrelation function. The Taylor microscale, λ_T, was estimated by fitting an osculating parabola at $t = 0$ of the autocorrelation function [33]. The time scales, T and λ_T, thus obtained were transformed into length scales, L and λ, using the local mean velocity of the flow, $\bar{u}$, according to Taylor's hypothesis of frozen turbulence, $\partial/\partial z \approx \partial/\partial t/\bar{u}$.

In these measurements the flow developed without the presence of the rod used to stabilise the flame. Whereas, in the near field the rod creates some flow disturbance, further downstream, where the flame images are acquired, the effect of the rod is largely non-existent, as observed previously, *e.g.* [34].

3.3 Particle image velocimetry

Two dimensional velocity measurements were performed with the particle image velocimetry (PIV) technique. The PIV system consisted of a diode pumped, dual-cavity, solid state Nd:YAG laser (EDGEWAVE, IS-611DE) and a PHOTRON Fastcam SA1.1 (LAVISION, HSS6). The camera was equipped with a CMOS sensor and capable of imaging at up to 5400 fps in full-frame mode (1024x1024). The laser was operated at 2 kHz producing 3 mJ/pulse at 532 nm (6 W average power in each channel) with a pulse duration of approximately 7.5 ns. The pulse separation for the PIV system was set to 20 μs for both the non-reacting and the reacting cases. The beam of approximately 5 mm by 3 mm was formed into an expanding light sheet by means of a concave cylindrical lens (f = -150 mm) and focused to a beam waist of around 0.7 mm with a convex cylindrical lens (f = 750 mm). The height of the light sheet was approximately 55 mm at the centreline of the burner, gradually increasing across the burner exit plane. Aluminium oxide particles (ALFA AESAR) with a nominal diameter of 3 μm were seeded into the air flow and the Mie scattered light of the particles was imaged onto the CMOS chip with a SIGMA 105 mm camera lens (f/2.8) with the f-stop set to 5.6. The camera, which had a 12-bit dynamic range, was operated at 4000 fps (*i.e.* 2000 double-images per second) in order to capture both PIV pulses. Due to the short exposure time of 250 μs per frame, chemiluminescence was not detected. Thanks to the 8GB onboard memory of the camera up to 2728 image pairs at full resolution were stored, which corresponded to total run durations of 1.36 s. A three-dimensional dot target (LAVISION TYPE 7) was used for image mapping, calibration and dewarping of the particle raw images. The velocity fields were calculated with a commercial multi-pass cross-correlation algorithm with adaptive window size (LAVISION DAVIS 7.2) decreasing from 64x64 pixels to 32x32 pixels with 50% overlap. This resulted in a vector spacing of 0.8 mm. The usable field of view was 45 x 45 mm.

The integral length scale was estimated from the spatial two-point correlation of the longitudinal velocity fluctuations for streamwise separations r in the direction of the longitudinal axis (z-axis),

$$g(r) = \overline{\big(u(z) - \overline{u(z)}\big)\big(u(z+r) - \overline{u(z+r)}\big)} / \overline{u(z)^2}, \quad (3)$$

integrated up to the first zero crossing. Due to the limited field of view, the autocorrelation function did not always decay to zero in which case $g(r)$ was integrated up to the end of the correlation function. For the estimation of the Taylor length scale an osculating parabola was fitted to the origin of the autocorrelation function [33],

$$\left|\frac{\mathrm{d}^2 g}{\mathrm{d}r^2}\right|_{r=0} = \frac{2}{\lambda^2}. \quad (4)$$

The integral and Taylor length scales calculated from the PIV data matched those calculated from the hot-wire data within 20%. The integral and Taylor length scale were calculated for each column of the PIV images in order to obtain the transverse profile of the turbulence length scales across the burner exit plane.

3.4 Conditioned particle image velocimetry

The flame front contours were extracted from the PIV seed particle images using the Conditioned Particle Image Velocimetry (CPIV) technique [35-37]. The technique observes the distinct step in particle number density due to the dilatation of the seeded gas as it passes through the flame front [38, 39]. With the help of an adaptive histogram-based intensity-threshold detection algorithm, flame front contours could be extracted from the particle number density gradient in the PIV particle raw images. Within the thin flame regime, the flame position and flame structure obtained with the CPIV technique have been shown to be sufficiently similar for the present purposes to that measured from local heat release rate distributions via CH-PLIF measurements [40]. The extracted contours were then represented parametrically in Cartesian coordinates, $x(s)$ and $y(s)$, as a function

of the path length parameter, s, of the contour and all subsequent flame contour quantities such as flame front normals and flame front curvatures, κ, were calculated from the parameterized contours. We used the processing procedure described in [41] for the extraction of the flame curvature, which results in the error of the local curvature value being within 10%.

4 Results and Discussion

4.1 Downstream development of turbulence

The local turbulence intensity, $u'/\bar{u}$, of the flow was obtained by decomposing the temporal hot-wire data into the time average velocity, $\bar{u}$, and the root-mean-squared velocity fluctuations, $\sqrt{\overline{u(t)^2}} = u'$, following Reynolds decomposition [33]. Figure 4 shows the downstream evolution of the turbulence intensity of all five grids between 50 mm and 300 mm. As can be seen, the RG, which had more than double the blockage ratio of the FGs, produced the largest turbulence level at around 50 mm downstream of the grid. The turbulence intensity, however, decays rapidly as the value of the downstream distance increases, following a power law decay of the form $u' \propto z^{-n}$ which is as expected for regular grid generated turbulence [1]. In contrast, the turbulence intensity of the FGs first increased over a large range of streamwise distances until it peaked and then decayed at a rate which was different from that of the regular turbulence grid. The position of maximum turbulence intensity could be shifted downstream by decreasing the blockage ratio, σ, or increasing the bar-width ratio, R_d, as can be seen by comparing the graphs for the FG1, FG2 and FG3. Similarly, the value of maximum turbulence intensity could be increased by increasing the blockage ratio and decreasing the bar-width ratio of the fractal grid. Thus, with the appropriate design parameters, a peak turbulence intensity similar to that of a regular grid could be achieved, but significantly further downstream of the grid.

These observations are similar to those obtained in previous wind tunnel experiments [3-5] for much larger grids.

The existence of the distinct turbulence production region of fractal grids can be explained by their fractal, or multi-scale, geometry [4]. In the case of fractal grids, various length scales are excited at the same time, producing wakes of different widths as shown schematically in Fig. 5. Smaller wakes reach their maximum turbulence intensity closer to the grid and the turbulence intensity would decay further downstream, if it were not for the next larger wakes to mix with these and help to increase turbulence. When all the differently sized wakes have finally mixed, the turbulence intensity reaches its maximum value at z_{peak}. Mazellier *et al.* [4] introduced a wake-interaction length scale, $z^* = l_0^{\,2} / d_0$, based on the wake of the largest square (with length l_0 and thickness d_0), which was used to demarcate the turbulence build-up region from the turbulence decay region. Their wind-tunnel studies showed, that the wake-interaction length scale, z^*, and the downstream position of maximum turbulence intensity, z_{peak}, are related by $z_{peak}/z^* \approx 0.45$. The location of maximum turbulence intensity is slightly over-predicted when using this relation, which can be attributed to the different size of their grids. However, the trend is predicted correctly. This can be seen in Fig. 4 by comparing the distributions for the FG2 and the FG4. Both grids were designed to have similar z^* values (see Table 1) and also produced the largest turbulence intensity at similar downstream positions.

In Fig. 6 the downstream development of the integral and the Taylor length scale is shown for a fractal grid and a regular grid. For clarity, only data of FG2 and RG are shown. Both the integral and the Taylor length scale of the RG increased with increasing values of the downstream position. This is commonly observed for regular grid generated turbulence [1]. The two length scales of the FG2, on the other hand, were almost constant over the entire range of streamwise distances. As both length scales remained constant

while the turbulence intensity decayed downstream, the downstream development of the turbulent Reynolds number, $\mathrm{Re}_t = u'L/\nu$, as well as the Taylor-based Reynolds number, $\mathrm{Re}_\lambda = u'\lambda/\nu$, had the same distinct rise and decay as observed for the turbulence intensity. This is interesting for two reasons. Firstly, a decaying turbulence at a constant length scale (either integral or Taylor) implies a direct departure from what is generally known for decaying Richardson-Kolmogorov turbulence where the energy dissipation rate, ε, is calculated via $\varepsilon = C_\varepsilon u'^3/L$ with $C_\varepsilon \approx \text{const}$ [42]. This was first noticed by Hurst *et al.* [3] and is extensively discussed in [4, 6] which is why we do not further comment on it here. Secondly, and maybe more important for combustion applications, it means that in principal the level of turbulence intensity can be chosen independently of the length scale of the flow by moving to different locations downstream of the fractal grid. This could be especially beneficial for combustion technology as will be explained later.

One way to describe this non-classical behaviour of turbulence decay is the idea of the so-called "self-preserving single length scale decay" [43, 44]. According to this concept, the energy spectra obtained at two different downstream positions (or two different Reynolds numbers) can be collapsed using one turbulence length scale (either Taylor or integral) as opposed to two turbulence length scales (*i.e.* the integral and Kolmogorov) in the case of conventional Richardson-Kolmogorov turbulence [45]. This particularity was pointed out in ref. [3, 5] and recently verified by Valente *et al.* [6] using extensive wind-tunnel data. In an attempt to demonstrate whether this behaviour can also be observed in our data, we followed the approach of Valente *et al.* [6] and plot in Fig. 7 the one-dimensional compensated energy spectra. The energy spectra were normalised with u' and λ for the two downstream locations of 150 mm and 210 mm which are denoted by 1 and 2, respectively. At these two downstream locations the ratio of the Taylor-based Reynolds number was similar for both types of

grids, $\left(\mathrm{Re}_{\lambda 1}/\mathrm{Re}_{\lambda 2}\right)_{\mathrm{RG}} \approx 1.4$ compared to $\left(\mathrm{Re}_{\lambda 1}/\mathrm{Re}_{\lambda 2}\right)_{\mathrm{FG}} \approx 1.3$, which indicates a similar decay of turbulence between 150 mm and 210 mm. The results for the RG and the FG2 are shown in Fig. 7a) and 7b), respectively. The one-dimensional energy spectra, $E(k)$, were calculated using [33],

$$E(k) = \frac{2}{\pi} u'^2 \int_0^\infty g(\tau) \cos(k\tau)\, d\tau \,. \tag{5}$$

It can be seen, that in the case of the RG, the energy spectra collapsed reasonably well for smaller frequencies but showed an increasing discrepancy toward larger frequencies. This is in line with Richardson-Kolmogorov turbulence where an outer and inner length scale is required to collapse both the large-scale and small-scale frequencies of the turbulence spectra [45]. The energy spectra of the FG2, on the other hand, showed a good collapse for all frequencies. This behavior is in agreement with previous measurements of fractal grid generated turbulence [3-6] and indicative of a single length scale decay [43, 44]. Recently however, Valente [46] pointed out that a purely visual validation of the concept is not sufficient to prove a single length scale decay of turbulence. In investigating the downstream decay of fractal grid generated turbulence with more scrutiny, he even finds that the use of two sets of length scales, L and η, may be more adequate to describe the turbulence decay behind fractal grids. Thus, to date it is unclear how the turbulence decay behind fractal grids should be described on a fundamental basis.

The fact remains, however, that the downstream decay of turbulence behind FGs is fundamentally different to what is currently known for grid generated turbulence and could potentially be beneficial for technical combustion applications. It would thus be interesting to investigate how this novel and unique flow field affects the structure of premixed flames. When comparing the flames it is, however, important not only to characterize the flow field at the centerline of the burner, as reported before, but across the

entire region of the flame. This is necessary as the differences between the flames, or lack thereof, could be - for example - due to an inhomogeneous velocity profile across the duct or due to variations of the integral length scale in the region of the flame investigation. In order to address these possibilities, the isotropy and homogeneity of the isothermal flow fields were investigated across the entire flame region which was used for the subsequent flame analysis.

4.2 Large-scale isotropy and homogeneity of the isothermal flow fields

One way to assess the large-scale isotropy of a flow field is the comparison of the root-mean-squared velocity fluctuations in longitudinal, u', and transversal direction, v'. No attempt was made to assess the small scale isotropy as reported by [6]. For an isotropic flow, the ratio, u'/v', which is known as the isotropy factor of the flow, should be equal to one [33]. Previous measurements of the isotropy factor in the wake of fractal grids showed values of 1.1 to 1.2 [3, 6, 47] for downstream distances, z/z_{peak}, similar to ours. Those measurements were predominantly performed on the centreline of the grid. In Fig. 8 the isotropy factors of the fractal grids FG2 and FG4 and the regular grid RG-50 are shown over the entire region (*yz*-plane) of the flame measurements (45 x 45 mm). Note that, the field of view started at the position of the flame stabilizing wire, *i.e.* for the FG2 and FG4 at $z_{\mathrm{wire}} = 180\,\mathrm{mm}$ and for the RG-50 at $z_{\mathrm{wire}} = 50\,\mathrm{mm}$. The isotropy factors thus obtained were between 0.9 and 1.2 for most of the field of view and similar to the centreline measurements [3, 6, 47], except for a small region in the lower left corner of the FG2 where the isotropy factor was larger than 1.2. This exception was probably caused by slightly inhomogeneous inflow conditions. Compared to the FG2, the flow field of the FG4 was more isotropic. This was expected as the FG4 had a larger number of fractal iterations which increased the homogeneity of the flow [3]. The RG-50, which is shown

for comparison, had a similar level of isotropy, but compared to the FGs was somewhat less homogeneous across the duct. This was probably caused by the fact that the field of view was only 7 mesh sizes away from the grid, which was necessary to achieve turbulence intensities similar to those of the FGs further downstream (see Fig. 4). As a consequence, at 7 mesh sizes downstream of the RG-50, the flow field might not have been fully developed. A more homogeneous distribution of the isotropy factor was observed for the RG-180. Overall, there was a similar level of large-scale isotropy produced by the FGs and the RG across the investigated field of view.

Flow homogeneity behind fractal grids was first investigated by Mazellier *et al.* [4] who compared velocities behind the openings of the grid with velocities behind the bars of the grid. The authors concluded that any inhomogeneities arising from the inhomogeneous distribution of the openings and the bars become negligible as soon as the flow enters the decay region of turbulence. This is in agreement with Valente *et al.* [6] who reported that during the entire decay region of turbulence, the streamwise rate of change of turbulence length scales was small compared to the length scales themselves, $\partial L/\partial z << L$. Again, both investigations were performed on the centreline of the grid.

In this study we assessed the homogeneity of the flow by the transverse profiles of the mean velocity, $\bar{u}$, the root-mean-squared velocity fluctuations, u', and the turbulence length scales, L and λ, across the burner exit plane. The profiles are shown in Fig. 8 for a downstream position of 10 mm above the flame stabilizing wire, as indicated by the dashed lines in the contours of the isotropy factor. This position was just upstream of the flame brush and also used to measure the flame properties later on. In all cases the velocity profiles were symmetric. The RG-50 had a flat velocity profile with some minor inhomogeneities due to the short distance downstream of the grid. The velocity profiles of the FGs showed a mild maximum on the centreline of the burner. This was due the

inhomogeneous distribution of openings and bars across the grid which caused a smaller pressure drop in the centre of the grid. The homogeneity of the velocity profiles could have been increased by increasing the number of fractal iterations, as performed in the case of the FG4 where the overshoot of centreline velocity was significantly reduced and the maximum and minimum mean velocities across the profile varied by less than 15%. Integrating the velocity profiles across the entire duct yielded the bulk velocity of 4 m/s.

Although the fractal geometry imposed a slightly inhomogeneous velocity distribution across the grid, there was only little variation of the integral and Taylor length scale across the duct. Especially in the case of the integral length scale, this variation could be attributed to the limited correlation length where the autocorrelation function did not always decay to zero. The Taylor length scale, which was calculated by fitting a parabola at the origin of the correlation function, was thus less affected by the limited field of view and hence was more uniform across the duct. Again, a more homogeneous transverse profile was achieved by increasing the number of fractal iterations, as can be seen by the profiles of the FG4. The transverse profiles of the RG-50 were also uniform.

In summary, it is noted that both types of grids produced a similar level of large-scale isotropy and flow homogeneity across the investigated field of view of 45 x 45 mm. Flow homogeneity downstream of the FGs could be further improved by increasing the number of fractal iterations, as shown for the FG4. It would have been desirable to use FGs with four iterations only, but due to the small burner width of 62 mm and manufacturing limitations this was not possible in this study.

4.3 Investigated flames

The first set of flame measurements was performed with the flame stabilizing wire at a downstream position of 180 mm. This position was chosen so that the flame was established in the turbulence decay region of the FGs to ensure a sufficiently

homogeneous and isotropic flow field and reasonably high turbulence intensity for the RG at the same time. However, at 180 mm the turbulence intensity of the RG was less than half of that produced by the FGs at the same downstream position, although the blockage ratio of the RG was almost twice as large. The RG-180 flames were therefore in a different combustion regime compared to the FG flames. This can be also seen from the combustion regime diagram [23, 31] in Fig. 9, where we plot the normalized velocity fluctuations, u'/s_l, against the normalized integral length scales, L/δ_l, of the flow for all investigated flames. Note that, the laminar burning velocities s_l = 0.15 m/s, 0.25 m/s and 0.33 m/s were obtained from Rozenchan *et al.* [48] and the thermal flame thickness δ_l = 0.68 mm, 0.55 mm and 0.48 mm from Lafay *et al.* [49] for ϕ = 0.7, 0.8 and 0.9, respectively. The velocity values for $\bar{u}$ and u' were taken from the non-reacting PIV data, 10 mm downstream of the wire. The integral length scale was taken from the centerline hot-wire measurements in non-reacting flow at the same downstream position. The three points of each grid from top to bottom correspond to ϕ = 0.7, 0.8 and 0.9, respectively.

In a second set of measurements the flame was stabilized 50 mm downstream of the RG. At this downstream position the level of turbulence intensity was similar to that of the FGs at 180 mm (see Fig. 4). By stabilizing the flames 50 mm downstream of the RG, the RG-50 flames and the FG flames were all in the same combustion regimes, *i.e.* in or near the corrugated flamelet regime. Note that, due to the smaller integral length scale, the RG-50 flames were further to the left in the Borghi-Peters diagram.

In the next sections the structure of the premixed flames are compared in terms of flame surface density, flame brush thickness, flame front curvature and turbulent burning velocity. The comparison was performed for flames with an equivalence ratio of ϕ = 0.7, except for the comparison of the turbulent burning velocities where we used all data to

generate more data points for correlations of turbulent burning velocity. The data used for the comparison is summarized in Table 2.

4.4 Flame surface density and brush thickness

The flame surface density (FSD), $\overline{\Sigma}$, describes the flame surface area per unit volume. In a predominantly two-dimensional flame the FSD can be calculated from the mean flame perimeter within a two-dimensional interrogation window as outlined in [50, 51]. The mean FSD was calculated from the planar CPIV measurements by integrating the continuous path length variable of the flame contours across an interrogation window of 0.8 mm by 0.8 mm, averaged over 2100 images.

In Fig. 10 the two dimensional distributions of the mean FSD are shown for the RG-180 and FG2. In the case of the FG2 a broad distribution of the FSD was observed with a width of around 5 mm near the flame anchor, rapidly increasing further downstream. The broad distribution of the FG2 indicates the large level of flame corrugation within the entire field of view of the CPIV measurements due to the high level of turbulence produced by the fractal grid. Compared to the FG2, the mean FSD distribution of the RG-180 flame appeared to be more confined throughout the entire field of view. Thus, it is noted that the FG2 produced a much more corrugated flame compared to the RG-180. This, however, was expected as the normalized velocity fluctuations, u'/s_l, of the FG2 at 180 mm downstream of the grid were 2.87, compared to 1.32 for the RG-180 (see Table 2).

In a next step, we extracted the transverse profiles of the mean FSD distribution for all six investigated flames (FG1-FG4, RG-180 and RG-50). Thus, the FG flames were also compared with the RG-50 flame which was subjected to normalized velocity fluctuations, u'/s_l, of 3.25, similar to those of the FG flames of around 3 (see Table 2). The FSD profiles were extracted 10 mm downstream of the flame anchor, which is the position

where the turbulence fields were characterized. The profiles were extracted normal to the $\bar{c} = 0.5$ iso-surface to normalize the different flame angles and shifted along the normal axis, η, in order for the FSD peaks to coincide at the same transverse position. The results for the left branch of the flame are given in Fig. 11. It is noted that the peak value of the mean FSD distribution, $\overline{\Sigma}_{\max}$, decreased with increase in turbulent velocity fluctuations, u'/s_l, as produced by the grids (see Table 2), and the mean FSD distribution broadened, which indicates an increased level of corrugation due to the higher levels of turbulence. This trend is well known for V-shaped flames and was previously reported by [51-55].

Interestingly, for similar values of u'/s_l, the flame produced by the FG3 and the flame produced by the RG-50 showed similar transverse profiles of mean FSD. This was surprising as it was expected that the unique turbulence field of the FGs and their interesting downstream development of the integral length scale may cause a different flame structure, for example by producing a larger FSD or an increased flame brush. This was clearly not the case.

However, the comparison performed so far was only at one downstream position and did not account for any evolution of the flames. As a consequence, in the next step the downstream development of the flame brush was investigated for all six flames. The flame brush thickness describes the average movement of the flame around its mean value and determines the spatial boundaries over which the turbulent flamelets are located. A different flame brush implies a different length scale of the flow which might also be associated with a different turbulent burning velocity of the flame. In order to quantify the downstream development of the flame brush thickness, transverse profiles of the mean FSD distribution similar to that in Fig. 11 were extracted normal to the $\bar{c} = 0.5$ iso-surface for both branches of the flame every 3 mm downstream of the flame anchor and fitted to the sum of two Gaussian distributions. The brush thickness, δ_T, was then defined as the

average of the widths of the two Gaussian distributions. Other authors [56, 57] have chosen to define the brush thickness as the perpendicular width between $\bar{c} = 0.1$ and $\bar{c} = 0.9$: at any rate, use of this alternative definition does not affect the conclusions reported here.

In Fig. 12a) the downstream development of brush thickness is shown for all six flames as a function of downstream distance above the wire. Similar to what was observed in the mean FSD images (see Fig. 10), the RG-180 flame had the smallest flame brush with a width of around 2.5 mm just above the wire. The brush increased linearly as the flame spread downstream of the anchor. A similar development was also observed for the FGs and the RG-50 flames, although their brush thicknesses were considerably larger than that of the RG-180 flame. The width of the brush also increased with increasing values of normalized velocity fluctuations, u'/s_l, similar to what was observed in Fig. 11 for the width of the FSD profiles.

The downstream development of brush thickness has been studied by many authors before, such as by ref. [57-60] in V-shaped flames, ref. [58, 61] in Bunsen type flames and ref. [62-64] in freely propagating spark ignition flames. All these references reported an increase of flame brush with increasing distance from the flame anchor or increasing time from the ignition event. Recently, the data on flame brush was reviewed by Lipatnikov *et al.* [30] who concluded that Taylor's theory of turbulent diffusivity [33] is an adequate way to describe the growth of the brush thickness,

$$\delta_T \propto (u' L t)^{1/2} \left\{ 1 - \frac{L}{u' t} \left(1 - \exp\left(\frac{-tu'}{L} \right) \right) \right\}. \quad (6)$$

In Eq. 6 t is the time from the ignition event, L is the integral length scale of the flow and u' is the root-mean-squared velocity fluctuations of the flow. For stationary flames, such

as V-shaped flames ref. [22, 30] pointed out that *t* can be replaced by the convective time, $t \approx z/\bar{u}$, following Taylor's hypothesis.

We fitted the mean flame brush data of our investigated flames to Eq. 6 and plot in Fig. 12b) the dimensionless brush thickness, δ_T/L, as a function of the dimensionless time, $t/(L/u')$. The mean flame brush data obtained from the six different flames collapsed to more or less a common development. The solid line, which represents the best fit of Eq. 6 to our data, predicted very well the growth of the flame brush with increasing distance from the flame holder for all six flames. It is also noted that the shape of the solid line is almost a straight line which implies that the flame brush grew linearly with time. This behavior was reported by other authors as well (see *e.g.* the references in [30]) and reflects the limiting case of convective times, $t \approx z/\bar{u}$, considerably less than the large eddy turnover time, L/u'. For this case Eq. 6 reduces to $\delta_T \propto u't$ and the growth of the brush no longer depends on the integral length scale of the flow [22, 30].

So far, according to data for mean FSD, flame brush thickness and its development downstream of the flame anchor, the fractal grid generated turbulence does indeed generate a more corrugated flame. However, the increase in flame corrugation can be described within the current framework of turbulent premixed flames. Therefore, the question remains whether the unique flow field of fractal grids has any additional, unnoticed effect on the flame. In this respect it would be wise to not only look at the large scale corrugation of the flame, as done in the case of the flame brush thickness, but to investigate the entire spectrum of flame wrinkles present in the corrugated flame front. In the next stage we therefore looked at the local flame front wrinkling. The question was whether for the same level of turbulence, flames in fractal grid generated turbulence cover the same range of wrinkles as flames in regular grid generated turbulence.

4.5 Flame front curvature

Local flame front wrinkling is best expressed in terms of flame front curvature, κ, as this quantity covers the whole spectrum of wrinkles observed in flames and not just large-scale wrinkles which account for most of the flame's corrugation. Additionally, the flame front curvature is calculated from instantaneous flame front contours and not by spatially averaging over a number of contours as in the case of mean FSD and flame brush. The flame front curvature therefore holds the potential to gain more insight into the local structure of flames and thus potentially reveals more subtle differences between them.

Flame front curvature values are usually calculated from the first and second order derivatives of the path length variable, s, along a flame contour. For a reasonably two-dimensional flame the curvature, κ, can be calculated from [65]

$$\kappa = \frac{\dot{x}(s)\ddot{y}(s) - \ddot{x}(s)\dot{y}(s)}{\left(\dot{x}(s)^2 + \dot{y}(s)^2\right)^{3/2}}. \qquad (7)$$

Here, $x(s)$ and $y(s)$ are the Cartesian coordinates of the flame contour as a function of the path length variable, s, as described in section 3.4.

Flame contour images are usually obtained by binarising laser induced fluorescence images [66-68], Mie scattering images [69], Rayleigh scattering images [70] or CPIV images [35, 37, 71]. During the process of binarisation, continuous flame contours get pixelated and this causes originally smooth contours to become less smooth [72]. Since the determination of curvature values requires the calculation of second order derivatives of the path length variable (compare Eq. 7), pixelation inherently affects the accuracy of the curvature values obtained. Different smoothing procedures are applied before the curvature calculation in order to filter the pixilation noise and obtain an approximately continuous contour again. Filters often used are the Savitzky-Golay filter [68], spatial filters [70, 73] or polynomial curve fits [74]. In each case the filtering

parameters such as the kernel size of the Savitzky-Golay filter or the order and length of the polynomial have to be adjusted appropriately as these affect the accuracy and range of curvature values obtained [72]. The most appropriate filter settings can be found by creating a pixelated version of an artificially created flame contour where the analytical solution of the curvature is known. The best filter settings are then defined as the settings which give the least deviation from the analytical curvature values over the entire range of curvature values assessed. Three test cases are widely used for optimizing the filter settings: a circle [68], a sine wave [70] and a rosette [72]. The rosette test curve [72] can be described as a circle with an oscillating single sinusoidal pattern and is arguably the most accurate test curve to date as it accounts for the undulating shape of the flame contour and provides a means of pixelating different curvature values differently [72].

Despite the advantages of the rosette test case over other test cases, the rosette does not yield a Gaussian like curvature distribution which is usually observed in turbulent premixed flames [64, 67]. In an attempt to overcome this shortcoming we modified the rosette test curve [72] and used a sum of sine waves instead of just one sine wave. The amplitudes of the sine waves were chosen such that the energy content of the sine waves followed a -5/3 decay, which is the decay rate of kinetic energy typically observed in turbulent flows [33]. By selecting a sufficient number of sine waves, 10 sine waves in our case, we obtained a modified rosette test curve which combined the advantages of Chrystie's test case [72] with a Gaussian like curvature distribution. Based on the modified rosette test curve a second order polynomial curve fit with a filter half-length of 9 pixels was chosen for smoothing the flame contour images. The deviation of the curve fit function from the theoretical curvature values of the test case was below 0.11 mm^{-1}.

Figure 13 shows the curvature distributions of the six investigated flames ($\phi = 0.7$) which were calculated from more than 4,000 contours. The bin size of the histograms was

0.1 mm^{-1}. In all six cases a symmetric distribution with a zero mean curvature was found. The curvature distributions showed a small bias toward positive curvature values (increasingly so for smaller values of u'/s_l), which indicates that there was only a minor effect of flame cusping [75]. The width of the distribution increased with increasing values of u'/s_l. Equally, the number of zero curvature values decreased with increasing values of u'/s_l which can be seen by comparing the curvature distributions of the weakly turbulent RG-180 flame with the intensely turbulent FG and RG-50 flames. The maximum absolute curvature values ranged from 1 mm^{-1} for the RG-180 flame to 2 mm^{-1} for the RG-50 and FG flames. This corresponds to flame radii of around 0.5 mm which are in the region of the magnitude of the laminar flame thickness δ_l. Finally, we also noted that for the same level of normalized velocity fluctuations, u'/s_l, the degree of flame wrinkling produced by the RG-50 and the FG3 was similar across the entire range of curvatures observed. The result in Fig. 13 therefore suggest that the flame front wrinkling in the presence of fractal grid generated turbulence is not different from that of "regular grid" generated turbulence, as long as both types of grids produced a similar level of normalized velocity fluctuations.

Thus, based on profiles of mean FSD distribution, downstream evolution of flame brush thickness and local flame wrinkling, we find that for a similar level of turbulence the corrugation of the flames in regular and fractal grid generated turbulence is in fact very similar. As a final parameter for investigating the possibility of a difference between flames in fractal and regular grid generated turbulence, we compared the turbulent burning velocity of all flames investigated here.

4.6 Turbulent burning velocity

The turbulent burning velocity, s_t, characterizes the rate at which reactants are consumed by the flame, larger values of s_t indicating higher burning rates of the flame. In

this study we measured the turbulent burning velocity of 18 V-shaped flames stabilized in the turbulence field of four fractal grids and one regular grid. The turbulent burning velocity ratio, s_t/s_l, was evaluated as a function of the normalized velocity fluctuations of the flow, u'/s_l, and correlations for the turbulent burning velocity were found.

As pointed out in the introduction, a suitable semi-empirical correlation of turbulent burning velocity is [23],

$$\frac{s_t}{s_l} = 1 + C\left(\frac{u'}{s_l}\right)^n, \tag{8}$$

which is a modification of Damköhler's [17] theory, $s_t/s_l \propto A_t/A_l$, and one of several possible expressions that have been derived during the years. The parameter *n* is determined from a best fit of Eq. 8 to the experimental data and expected to be close to 0.5 [22, 30]. The parameter *C* is expected to be proportional to L/δ_l [31] or a function of the turbulent Reynolds number [22, 30], as previously explained. If Eq. 8 represents a suitable correlation of turbulent burning velocity, then a least-square fit of Eq. 8 to our experimental values of s_t/s_l should show a reasonably good collapse for flames in regular and fractal grid generated turbulence.

We followed this idea and determined the turbulent burning velocity from the mean half-angle of the V-shaped flame, α, and the local mean velocity of the approaching flow, $\bar{u}$, using, $s_t = \bar{u}\sin\alpha$ [23]. The mean flame angle was determined as that between the $\bar{c} = 0.5$ iso-surfaces of the left and right branch of the flame and the mean velocity was taken from the average velocity profiles just ahead of the flame brush as given in Table 2. We used the mean progress variable distribution to calculate the flame angle. We utilized the portion of the flame near the flame stabilization location, where the flame angle is largely constant. The data was then normalized with the laminar burning velocity

as given by Rozenchan [48] and a least-square fit of Eq. 8 was applied to the experimental data. The estimation of the turbulent burning velocity using the flame half angle assumes that all the reactants are consumed within the flame. At times this is not the case in V-flames, so that the absolute value of the turbulent flame speed could be biased, due to differences in the velocity $\bar{u}$. However, we don't expect the level of this bias to affect the form of the correlations we present and for comparison with other studies, *e.g.* [76], we keep the above definition.

In Fig. 14a) the turbulent burning velocity of all 18 investigated flames shows that the burning velocity ratio s_t/s_l increased with u'/s_l . The experimental data could be collapsed using $s_t/s_l = 1+4.59(u'/s_l)^{0.49}$, which represents the best fit of Eq. 8 to the data and is indicated by the solid line in Fig. 14a). The exponent of the correlation was close to Damköhler's proposed value of 0.5, which was expected, and the parameter *C* was a constant. It is also noted that no length scale dependency was needed to collapse our data, as can be seen in Fig. 14b) more clearly. In fact, when choosing a correlation with the two dimensionless groups Re_t and u'/s_l , the experimental data was best represented by $s_t/s_l = 1+6.75\,\mathrm{Re}_t^{-0.08}(u'/s_l)^{0.5}$, which implies that u'/s_l was the dominant factor in the correlation and the length scale dependency of the turbulent burning velocity was negligible in our flames. A similar trend was observed when the Taylor-based Reynolds number or the length-scale ratio L/δ_L were chosen instead of the turbulent Reynolds number. Then, the best correlations were $s_t/s_l = 1+6.75\,\mathrm{Re}_\lambda^{-0.11}(u'/s_l)^{0.52}$ and $s_t/s_l = 1+6.43(L/\delta_l)^{-0.12}(u'/s_l)^{0.45}$, respectively. Moreover, by choosing a Reynolds dependency such as $s_t/s_l = 1+A\cdot\mathrm{Re}_t^{0.25}(u'/s_l)^n$, as for example suggested by Gülder [26, 28], the experimental data did not collapse.

It is interesting that our experimental data of the turbulent burning velocity could be collapsed without the length scale information of the flow field. Therefore, we performed a literature review as to the role of the integral scale L in current correlations of turbulent burning velocity. In the review paper by Lipatnikov [30], one section is dedicated to this topic. He finds that various authors [28, 31, 77-79] use different expressions for the turbulent burning velocity as a function of the integral scale, ranging from $s_t \propto L^{0.17}$ to $s_t \propto L^{0.5}$. He concludes that, due to this large scatter of correlations, the influence of L on s_t is currently unclear and he therefore recommends a more thorough investigation. Driscoll [22] comes to a similar conclusion and assumes the discrepancy is partly due to the experimental procedure by which correlations of the turbulent burning velocity are established. For example, often the integral length scale cannot be changed without changing other parameters as well, such as the level of turbulence. Moreover, often the length scale is only measured at one specific location of the experiment, such as the exit plane of the burner or the center of an ignition bomb, and not at the location of the actual flame brush.

When it comes to correlations of the turbulent burning velocity, they are generally two ways to measure the turbulent burning velocity as a function of the reactants' flow field. One way is to use a combustion bomb [23] where the turbulent flow field inside the bomb is created with the help of two or four mutually opposed fans. A flame is initiated by a spark in the centre of the vessel and the subsequent propagation of the spherical flame is monitored. The rate of change of flame diameter is then defined as the turbulent burning velocity. Advantages of the combustion bomb are, apart from needing no explicit method of anchoring the flame, the ability of studying transient flame phenomena, flame propagation under elevated pressure and the possibility of covering a large range of length scales. The latter is particularly useful for correlations of turbulent burning velocity, which

is why many of the databases [19, 20, 26, 80] contain a considerable amount of experimental data obtained from combustion bombs. One disadvantage of the combustion bomb is, however, the determination of the turbulence length scale. It is usually inferred from the rotational speed of the fan based on a previously recorded calibration which has been established at a specific point inside the combustion bomb [81]. The spatial distribution of the turbulence length scale is often not known and the length scale, which has been assigned to the turbulent burning velocity, might therefore deviate from the length scale at the position of the actual flame brush. A second disadvantage of the combustion bomb is that the turbulence length scale cannot be changed independently from the root-mean-squared velocity fluctuations of the flow, u', since both quantities are determined by the rotational speed of the fan. The length scale dependency of the turbulent burning velocity might therefore as well be the combined effect of L and u'.

A second way to determine correlations of turbulent burning velocity is the investigation of stationary flames such as stagnation plane flames, rim stabilized flames or V-shaped flames, which have been stabilized in a turbulent flow field. Usually grids or perforated plates are used to produce a turbulent flow field with well-defined parameters. In grid generated turbulence, the integral scale is proportional to the mesh size of the grid and does not depend on the mean flow through the grid, whereas the root-mean-squared velocity fluctuations change with changing mean flows. Therefore, in grid generated turbulence, the integral length scale can in principle be varied independently from the root-mean-squared velocity fluctuations. The influence of L on s_t could, for example, be investigated by recording the turbulent burning velocity for various mean flow rates over a series of grids. However, previous designs of turbulence grids allowed for only a small change of L for sufficiently high levels of turbulence, $u' \geq s_l$. Previous authors [82-84], who used regular grids as turbulence generators for correlations of turbulent burning

velocity, varied the turbulence length scale between 1 mm and 2 mm, as opposed to 20 mm or 30 mm in the case of combustion bombs. For example, Smith [84] used two sets of grids which produced integral scales of 0.6 mm and 1.6 mm and reported a length scale dependency of $s_t \propto L^{0.5}$ (although during his analysis he used the turbulent Reynolds number $u'L/\nu$ instead of L itself). Shepherd *et al.* [83] used two grids which produced a turbulence length scale of 3.1 mm and 4.7 mm and reported a decrease of s_t by L when u' was kept constant and Li *et al.* [82] used two meshes with a mesh size of 4 mm and 6 mm and reported an increase of s_t by L, although no specific exponent was given. A wider range of turbulence length scales (between 5 mm and 18 mm) was finally studied by Liu [85]. He investigated a total of seven perforated plates with orifice diameters ranging from 1 mm to 18 mm and reported a dependency of the turbulent burning velocity on u' only, despite the large variation of the integral scale. It should be noted, however, that the root-mean-squared velocity fluctuations were below the laminar burning velocity of the flame, $u' \leq s_l$, in the case of large integral scales.

In our experiments, the integral length scale varied between 4 mm (RG-50) and 8.3 mm (FG4), which is a wider range of length scales than most of the previous studies where turbulence grids were used. Therefore, it is interesting that our experimental data could be collapsed without the length scale information of the flow, despite varying widely the flow length scales.

Based on our findings and the literature review presented above, we believe that the influence of the turbulence length scale on the turbulent burning velocity is currently unclear, unlike the influence of the normalized velocity fluctuations, u'/s_l, where an exponent of 0.5 is usually reported [19, 28, 30] and was also measured here. A more specific investigation of the effect of L on s_t is therefore desirable.

It must be mentioned though, that the turbulent burning velocity was not the only flame parameter in the present investigations where the integral length scale did not seem to have an effect. For example, the downstream development of the flame brush thickness did not show a length scale dependency either, as can be seen by the almost linear shape of the solid line in Fig. 10b), indicating a linear growth of the flame brush thickness with the root-mean-squared velocity fluctuations, $\delta_T \propto u't$, independent of the integral scale of the flow. Similarly, the curvature distributions (Fig. 4.13) of the RG-50 ($u'/s_l = 3.25$, L = 4 mm) and FG3 ($u'/s_l = 3.10, L$ = 8.2 mm) were almost identical, although both flames were subjected to very different integral scales. It would thus be interesting to investigate the reasons behind this apparently negligible effect of the length scale on certain flame parameters.

It is instructive to compare the values of the measured turbulent flame speed to the respective values measured in other experiments, utilising fractal grids. Fractal cross grids were installed in an opposed jet flow configuration [13] to generate turbulent fluctuations and the same definition of the turbulent burning velocity as here was used. For CH_4 and equivalence ratio 0.8 the normalised turbulent flame speed was S_T/S_L=8.4-9.8 (depending on the measurement process) corresponding to u'/S_L=3.6 and for equivalence ratio 0.9 the respective values were S_T/S_L=7.8-8.0 for u'/S_L=2.8. These values fall within the correlation of the turbulent burning velocity presented in Fig. 14a. Fractal cross grids were also installed in a round swirl burner [12], where a correlation of the turbulent consumption burning speed gave values ~1/3 of the values measured here, for the same normalized turbulent velocity. However, they use a different definition of the burning velocity than here and similar differences have been observed before [22]. We should point out that these experiments used fractal cross grids rather than fractal square grids as used here. We used fractal square grids to tailor the development of turbulence to our

experimental setup, given differences in downstream mixing and turbulence decay between the different grid patterns, *e.g.* [3].

To facilitate further comparison to other experimental data we plot the dependence of the turbulent burning velocity against the Karlovitz number, as, for example, in [76]. Figure 15 shows this dependence, where we used the same definition of the Karlovitz number, and we found a similar power law reduction of s_t with the Karlovitz number, albeit with a different exponent (-0.348).

5. Conclusions

The effect of fractal grid generated turbulence on the structure of premixed V-shaped flames of methane and air was studied. A set of four low blockage ($\sigma \approx 35\%$) fractal square grids was designed where the blockage ratio, the bar-width ratio or the number of fractal iterations was changed. For comparison also a regular square grid with 60% blockage ratio was designed.

Our findings can be summarized as follows:

- The turbulent flame speed correlation presented in Fig. 14 reveals no length scale dependence. A literature review showed that the influence of the turbulence length scale on the turbulent burning velocity is currently unclear, unlike the influence of the normalized velocity fluctuations, u'/s_l, where an exponent of 0.5 is usually reported [19, 28, 30]. Moreover, many of the existing correlations which infer a length scale dependency of the turbulent burning velocity are based on experimental data obtained in combustion bombs where the influence of the length scale can only be investigated in terms of the turbulent Reynolds number, $\mathrm{Re}_t = u'L/\nu$ and not in terms of the integral scale L itself.

- Flames that were stabilized in the turbulent flow field of the fractal grids showed more intense corrugation, larger flame front wrinkling and larger turbulent burning velocities compared to flames stabilized at the same downstream position in regular grid generated turbulence. This demonstrates the potential benefits of using fractal grids as a new type of turbulence generators in premixed combustion.
- When compared for the same turbulence level however, it was found that the flames in fractal grid generated turbulence produced a similar degree of flame corrugation, flame front wrinkling and similar turbulent burning velocities compared to flames in regular grid generated turbulence. In particular, it could be demonstrated that the mean flame brush thickness as well as its growth downstream of the flame holder can be predicted by Taylor's theory of turbulent diffusivity. The mean flame surface density profiles as well as the probability density functions of the local flame front wrinkling were similar for a similar level of turbulence. It could also be shown that the increase in turbulent burning velocity can be explained by Damköhler's theory of premixed flame propagation. The best fit to our experimental data on the turbulent burning velocity was $s_t/s_l = 1 + 4.59(u'/s_l)^{0.49}$ and revealed no length scale dependency of the turbulent burning velocity for our flames.
- In light of these findings the use of turbulence grids for studies of the turbulent burning velocity seems a promising approach, because the length scale of the flow can be changed independently of the root-mean-squared velocity fluctuations of the flow, u'. Previous grid designs, however, could not generate a large range of integral length scales for a sufficiently

turbulent flow, as opposed to the combustion bomb. In this context, fractal grids seem to be helpful as they produce a high level of turbulence and cover a wide range of turbulence length scales at the same time. Moreover, the geometry of the fractal grids allows for more optimization flexibility compared to current grids. Thus, fractal grids, which are particularly suited for the investigation of s_t as a function of L, can be designed. Another potential advantage of fractal grids is the fact that the turbulence length scales remained almost constant over a long distance downstream of the grid (cf. Fig. 6) whereas the root-mean-squared velocity fluctuations of the flow varied according to the turbulence intensity (cf. Fig 4). The effect of the integral scale on the turbulent burning velocity could therefore also be investigated by stabilizing the flame at different downstream positions of the grid.

Based on the experimental findings and the discussion presented above we propose the use of fractal grids as a new type of turbulence generators for premixed combustion applications. Fractal grids produce larger turbulence levels than regular grids over a well-defined downstream region and at a relatively low cost in terms of pressure drop. Moreover, theories which have been established for homogeneous isotropic turbulence based on regular grids are readily applicable to flames in fractal grid generated turbulence. Thus, fractal grids could pave the way for future, more power dense combustors.

Acknowledgements

The authors would like to acknowledge financial support of the EU LIMOUSINE project, a Marie Curie Initial Training Network Project of the FP7 program under grant number 214905 and from EPSRC grant EP/G01597X/1.

References

1. **Comte-Bellot, G. and S. Corrsin, *The use of a contraction to improve the isotropy of grid-generated turbulence.* Journal of Fluid Mechanics, 1966. 25(04): p. 657-682.**

2. **Filatyev, S.A., et al., *Measured properties of turbulent premixed flames for model assessment, including burning velocities, stretch rates, and surface densities.* Combustion and Flame, 2005. 141(1-2): p. 1-21.**

3. **Hurst, D. and J.C. Vassilicos, *Scalings and decay of fractal-generated turbulence.* Physics of Fluids, 2007. 19(3).**

4. **Mazellier, N. and J.C. Vassilicos, *Turbulence without Richardson–Kolmogorov cascade.* Physics of Fluids, 2010. 22(7): p. 075101.**

5. **Seoud, R.E. and J.C. Vassilicos, *Dissipation and decay of fractal-generated turbulence.* Physics of Fluids, 2007. 19(10).**

6. **Valente, P.C. and J.C. Vassilicos, *The decay of turbulence generated by a class of multiscale grids.* Journal of Fluid Mechanics, 2011. 687: p. 300-340.**

7. **Nedic, J., et al., *Aeroacoustic Performance of Fractal Spoilers.* Aiaa Journal, 2012. 50(12): p. 2695-2710.**

8. **Cafiero, G., S. Discetti, and T. Astarita, *Heat transfer enhancement of impinging jets with fractal-generated turbulence.* International Journal of Heat and Mass Transfer, 2014. 75: p. 173-183.**

9. **Laizet, S. and J.C. Vassilicos, *Stirring and scalar transfer by grid-generated turbulence in the presence of a mean scalar gradient.* Journal of Fluid Mechanics, 2015. 764: p. 52-75.**

10. **Suzuki, H., et al., *Direct numerical simulation of turbulent mixing in regular and fractal grid turbulence.* Physica Scripta, 2010. T142.**

11. **Manshoor, B., F. Nicolleau, and S.B.M. Beck, *The fractal flow conditioner for orifice plate flow meters.* Flow Measurement and Instrumentation, 2011. 22(3): p. 208-214.**

12. **Verbeek, A.A., et al., *Fractal turbulence enhancing low-swirl combustion.* Combustion and Flame, 2015. 162(1): p. 129-143.**

13. **Goh, K.H.H., P. Geipel, and R.P. Lindstedt, *Lean premixed opposed jet flames in fractal grid generated multiscale turbulence.* Combustion and Flame, 2014. 161(9): p. 2419-2434.**

14. **Soulopoulos, N., et al., *Turbulent premixed flames on fractal-grid-generated turbulence.* Fluid Dynamics Research, 2013. 45(6).**

15. **Vassilicos, J.C., *Dissipation in Turbulent Flows.* Annual Review of Fluid Mechanics, 2015. 47(1): p. 95-114.**

16. **Mazellier, N., L. Danaila, and B. Renou, *Multi-Scale Turbulence Injector: a new tool to generate intense homogeneous and isotropic turbulence for premixed combustion.* Journal of Turbulence, 2010. 11(43): p. 1-30.**

17. **Damköhler, G., *The effect of turbulence on the flame velocity in gas mixtures.* Z. Elektrochem. Angew. Phys. Chem., 1940. 46: p. 601-626.**

18. **Bray, K.N.C., *Studies of the Turbulent Burning Velocity.* Proc. R. Soc. Lond. A, 1990. 431(1882): p. 315-335.**

19. **Bradley, D., *How fast can we burn?* Symposium (International) on Combustion, 1992. 24(1): p. 247-262.**

20. **Abdel-Gayed, R.G., D. Bradley, and M. Lawes, *Turbulent burning velocities: A general correlation in terms of straining rates.* Proceedings of the Royal Society of London. Series A, Mathematical and Physical Sciences, 1987. 414(1847): p. 389-413.**

21. **Abdel-Gayed, R.G. and D. Bradley, *Criteria for turbulent propagation limits of premixed flames.* Combustion and Flame, 1985. 62(1): p. 61-68.**

22. **Driscoll, J.F., *Turbulent premixed combustion: Flamelet structure and its effect on turbulent burning velocities.* Progress in Energy and Combustion Science, 2008. 34(1): p. 91-134.**

23. **Peters, N., *Turbulent Combustion*. 2004, Cambridge: Cambridge University Press.**

24. **Gouldin, F.C., *An application of fractals to modeling premixed turbulent flames.* Combustion and Flame, 1987. 68(3): p. 249-266.**

25. **Kerstein, A.R., *Fractal Dimension of Turbulent Premixed Flames.* Combustion Science and Technology, 1988. 60(4-6): p. 441-445.**

26. **Gülder, Ö.L., *Turbulent premixed flame propagation models for different combustion regimes.* Symposium (International) on Combustion, 1991. 23(1): p. 743-750.**

27. **Peters, N., *Laminar flamelet concepts in turbulent combustion.* Symposium (International) on Combustion, 1988. 21(1): p. 1231-1250.**

28. **Gülder, Ö.L., *Turbulent premixed combustion modelling using fractal geometry.* Symposium (International) on Combustion, 1991. 23(1): p. 835-842.**

29. **Gülder, Ö.L., *Fractal characteristics and surface density of flame fronts in turbulent premixed combustion.* Mediterranian Combustion Symposium-99, 1999: p. 130-154.**

30. **Lipatnikov, A.N. and J. Chomiak, *Turbulent flame speed and thickness: phenomenology, evaluation, and application in multi-dimensional simulations.* Progress in Energy and Combustion Science, 2002. 28(1): p. 1-74.**

31. **Peters, N., *The turbulent burning velocity for large-scale and small-scale turbulence.* Journal of Fluid Mechanics, 1999. 384(-1): p. 107-132.**

32. Zimont, V. and V. Battaglia, *Joint RANS/LES Approach to Premixed Flame Modelling in the Context of the TFC Combustion Model.* Flow Turb. Combust., 2006. 77(1): p. 305-331.

33. Pope, S.B., *Turbulent flows*. 2000: Cambridge University Press.

34. Kheirkhah, S. and Ö.L. Gülder, *Consumption speed and burning velocity in counter-gradient and gradient diffusion regimes of turbulent premixed combustion.* Combustion and Flame, 2014(0).

35. Pfadler, S., et al., *High resolution dual-plane stereo-PIV for validation of subgrid scale models in large-eddy simulations of turbulent premixed flames.* Combust. Flame, 2009. 156(8): p. 1552-1564.

36. Pfadler, S., et al., *Direct evaluation of the subgrid scale scalar flux in turbulent premixed flames with conditioned dual-plane stereo PIV.* Proc. Combust. Inst., 2009. 32: p. 1723-1730.

37. Pfadler, S., A. Leipertz, and F. Dinkelacker, *Systematic experiments on turbulent premixed Bunsen flames including turbulent flux measurements.* Combust. Flame, 2008. 152(4): p. 616-631.

38. Pfadler, S., et al., *Measurement of the conditioned turbulence and temperature field of a premixed Bunsen burner by planar laser Rayleigh scattering and stereo particle image velocimetry.* Exp. Fluids, 2005. 39(2): p. 375-384.

39. Steinberg, A.M., J.F. Driscoll, and S.L. Ceccio, *Temporal evolution of flame stretch due to turbulence and the hydrodynamic instability.* Proc. Combust. Inst., 2009. 32(2): p. 1713-1721.

40. Steinberg, A., J. Driscoll, and S. Ceccio, *Measurements of turbulent premixed flame dynamics using cinema stereoscopic PIV.* Exp. Fluids, 2008. 44(6): p. 985-999.

41. Bayley, A., Y. Hardalupas, and A.K.P. Taylor, *Local curvature measurements of a lean, partially premixed swirl-stabilised flame.* Experiments in Fluids, 2012. 52(4): p. 963-983.

42. Frisch, U., *Turbulence. The legacy of A.N. Kolmogorov*. 1995: Cambridge University Press.

43. George, W.K., *The decay of homogeneous isotropic turbulence.* Phys. Fluids A, 1992. 4(7): p. 1492-1509.

44. George, W.K. and H.L. Wang, *The exponential decay of homogeneous turbulence.* Phys. Fluids, 2009. 21(2).

45. Kolmogorov, A.N., *The local structure of turbulence in incompressible viscous fluid for very large Reynolds.* Dokl. Akad. Nauk SSSR, 1941. 30(4): p. 299-303.

46. Valente, P.C., *Energy transfer and dissipation in equilibrium and nonequilibrium turbulence*, in *Department of Aeronautics*2013, Imperial College London.

47. Gomes-Fernandes, R., B. Ganapathisubramani, and J.C. Vassilicos, *Particle image velocimetry study of fractal-generated turbulence.* Journal of Fluid Mechanics, 2012. 711: p. 306-336.

48. Rozenchan, G., et al., *Outward propagation, burning velocities, and chemical effects of methane flames up to 60 ATM.* Proceedings of the Combustion Institute, 2002. 29: p. 1461-1470.

49. Lafay, Y., et al., *Experimental and numerical investigation of the effect of H-2 enrichment on laminar methane-air flame thickness.* Combustion and Flame, 2008. 153(4): p. 540-561.

50. Deschamps, B.M., et al., *Surface density measurements of turbulent premixed flames in a spark-ignition engine and a bunsen-type burner using planar laser-induced fluorescence.* Symposium (International) on Combustion, 1996. 26(1): p. 427-435.

51. Veynante, D., J.M. Duclos, and J. Piana, *Experimental analysis of flamelet models for premixed turbulent combustion.* Symposium (International) on Combustion, 1994. 25(1): p. 1249-1256.

52. Shepherd, I.G., *Flame surface density and burning rate in premixed turbulent flames.* Symposium (International) on Combustion, 1996. 26(1): p. 373-379.

53. Veynante, D., et al., *Experimental analysis of flame surface density models for premixed turbulent combustion.* Symposium (International) on Combustion, 1996. 26(1): p. 413-420.

54. Domingo, P., et al., *DNS of a premixed turbulent V flame and LES of a ducted flame using a FSD-PDF subgrid scale closure with FPI-tabulated chemistry.* Combustion and Flame, 2005. 143(4): p. 566-586.

55. Lam, J.S.L., et al., *On the high-resolution modelling of a turbulent premixed open v-flame.* Combust. Theory Modelling, 2003. 7(1): p. 1-28.

56. Vena, P.C., et al., *Equivalence ratio gradient effects on flame front topology in a stratified iso-octane/air turbulent V-flame.* Proceedings of the Combustion Institute, 2011. 33(1): p. 1551-1558.

57. Gouldin, F.C. and P.C. Miles, *Chemical closure and burning rates in premixed turbulent flames.* Combustion and Flame, 1995. 100(1–2): p. 202-210.

58. Cheng, R.K. and I.G. Shepherd, *The influence of burner geometry on premixed turbulent flame propagation.* Combustion and Flame, 1991. 85(1–2): p. 7-26.

59. Rajan, S., J.R. Smith, and G.D. Rambach, *Internal structure of a turbulent premixed flame using Rayleigh scattering.* Combustion and Flame, 1984. 57(1): p. 95-107.

60. Kheirkhah, S. and Ö.L. Gülder, *Topology and Brush Thickness of Turbulent Premixed V-shaped Flames.* Flow, Turbulence and Combustion, 2014. 93(3): p. 439-459.

61. **Cheng, R.K., I.G. Shepherd, and L. Talbot,** ***Reaction rates in premixed turbulent flames and their relevance to the turbulent burning speed.*** **Symposium (International) on Combustion, 1989. 22(1): p. 771-780.**

62. **Goix, P., P. Paranthoen, and M. Trinite,** ***A tomographic study of measurements in a V-shaped H2□air flame and a lagrangian interpretation of the turbulent flame brush evolution.*** **Combustion and Flame, 1990. 81(3–4): p. 229-241.**

63. **Renou, B., et al.,** ***Characterization of the local flame structure and the flame surface density for freely propagating premixed flames at various Lewis numbers.*** **Combustion Science and Technology, 2002. 174(4): p. 143-179.**

64. **Renou, B., E. Samson, and A. Boukhalfa,** ***An experimental study of freely propagating turbulent propane/air flames in stratified inhomogeneous mixtures.*** **Combustion Science and Technology, 2004. 176(11): p. 1867-1890.**

65. **Bronshtein, I.N., et al.,** ***Handbook of Mathematics*****. Vol. 5th Edition. 2007, Heidelberg: Springer.**

66. **Soika, A., F. Dinkelacker, and A. Leipertz,** ***Pressure influence on the flame front curvature of turbulent premixed flames: comparison between experiment and theory.*** **Combustion and Flame, 2003. 132(3): p. 451-462.**

67. **Ayoola, B.O., et al.,** ***Spatially resolved heat release rate measurements in turbulent premixed flames.*** **Combust. Flame, 2006. 144(1-2): p. 1-16.**

68. **Haq, M.Z., et al.,** ***Wrinkling and curvature of laminar and turbulent premixed flames.*** **Combust. Flame, 2002. 131(1-2): p. 1-15.**

69. **Lachaux, T., et al.,** ***Flame front analysis of high-pressure turbulent lean premixed methane–air flames.*** **Proc. Combust. Inst., 2005. 30(1): p. 819-826.**

70. **Chen, Y.C.,** ***Measurements of flame-front curvature based on Fourier transformation.*** **Combust. Theory Modelling, 2007. 11(3): p. 333-349.**

71. **Pfadler, S., F. Beyrau, and A. Leipertz,** ***Flame front detection and characterization using conditioned particle image velocimetry (CPIV).*** **Opt. Express, 2007. 15(23): p. 15444-15456.**

72. **Chrystie, R.S.M., et al.,** ***On the improvement of two-dimensional curvature computation and its application to turbulent premixed flame correlations.*** **Meas. Sci. Technol., 2008. 19(12): p. 125503.**

73. **Gashi, S., et al.,** ***Curvature and wrinkling of premixed flame kernels—comparisons of OH PLIF and DNS data.*** **Proc. Combust. Inst., 2005. 30(1): p. 809-817.**

74. **Renou, B., et al.,** ***Local scalar flame properties of freely propagating premixed turbulent flames at various Lewis numbers.*** **Combust. Flame, 2000. 123(4): p. 507-521.**

75. **Lee, T.W., G.L. North, and D.A. Santavicca,** ***Surface properties of turbulent premixed propane/air flames at various Lewis numbers.*** **Combust. Flame, 1993. 93(4): p. 445-456.**

76. **Guo, H.S., et al., *Burning rates and surface characteristics of hydrogen-enriched turbulent lean premixed methane-air flames.* International Journal of Hydrogen Energy, 2010. 35(20): p. 11342-11348.**

77. **Liu, Y., M. Ziegler, and B. Lenze, *Burning velocity of premixed flames as a function of turbulence and physico-chemical fuel properties.* Proceedings Joint Meeting of the British-German Sections of the Combustion Institute, 1993: p. 64-67.**

78. **Williams, D.T. and L.M. Bollinger, *The effect of turbulence on flame speeds of Bunsen-type flames.* Symposium on Combustion and Flame, and Explosion Phenomena, 1949. 3(1): p. 176-185.**

79. **Wohl, K. and L. Shore, *Experiments with Butane-Air and Methane-Air Flames.* Industrial & Engineering Chemistry, 1955. 47(4): p. 828-834.**

80. **Bradley, D., et al., *Turbulent burning velocity, burned gas distribution, and associated flame surface definition.* Combustion and Flame, 2003. 133(4): p. 415-430.**

81. **Abdel-Gayed, R.G., K.J. Al-Khishali, and D. Bradley, *Turbulent Burning Velocities and Flame Straining in Explosions.* Proc. R. Soc. Lond. A, 1984. 391(1801): p. 393-414.**

82. **Li, S.C., P.A. Libby, and F.A. Williams, *Experimental investigation of a premixed flame in an impinging turbulent stream.* Symposium (International) on Combustion, 1994. 25(1): p. 1207-1214.**

83. **Shepherd, I.G., et al., *The burning rate in turbulent bunsen flames.* Symposium (International) on Combustion, 1998. 27(1): p. 909-916.**

84. **Smith, K.O. and F.C. Gouldin, *Turbulence effects on flame speed and flame structure.* Aiaa Journal, 1979. 17(11): p. 1243-1250.**

85. **Liu, Y. and B. Lenze, *The influence of turbulence on the burning velocity of premixed CH4-H2 flames with different laminar burning velocities.* Symposium (International) on Combustion, 1989. 22(1): p. 747-754.**

Figures

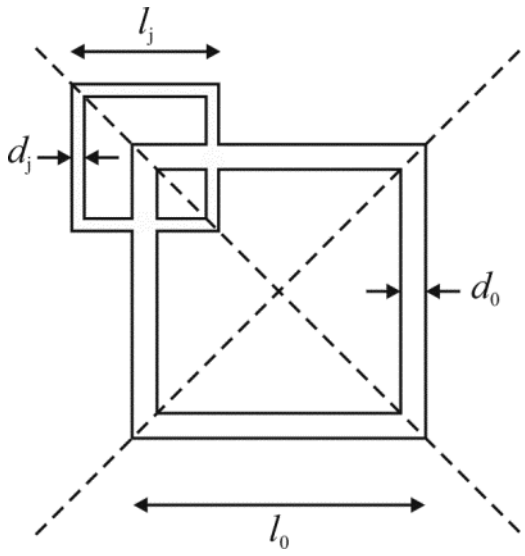

Fig. 1: Schematic of the fractal geometry for the 0^{th} and j^{th} iteration.

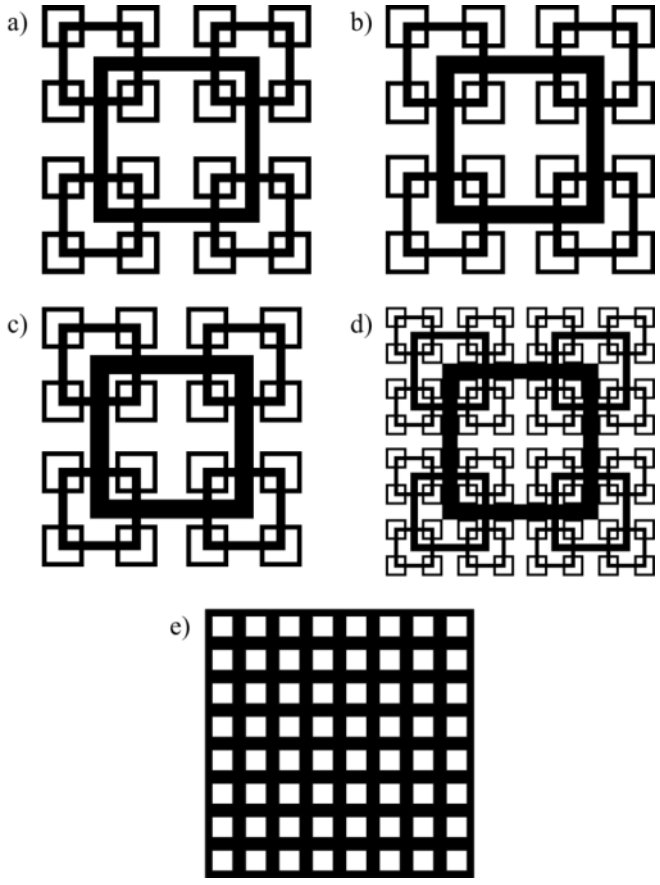

Fig. 2: Schematics of the investigated grids: a) FG1, b) FG2, c) FG3, d) FG4, e) RG.

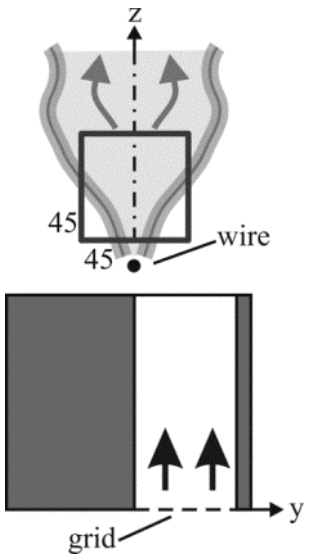

Fig. 3: Schematic of the burner with the field of view of the measurements.

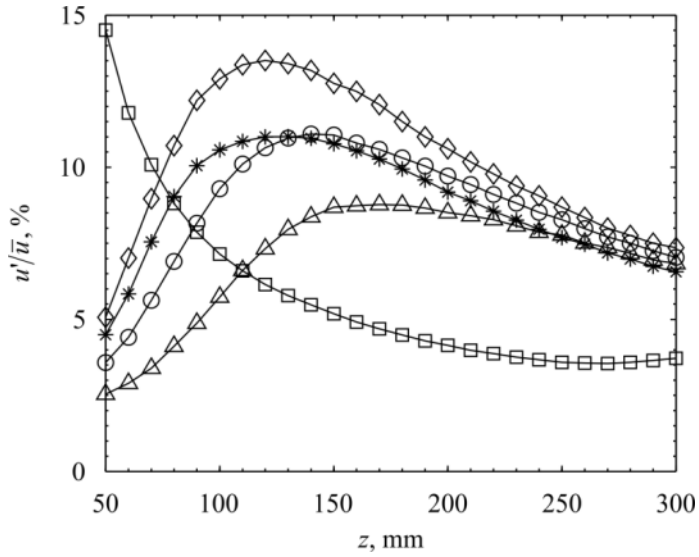

Fig. 4: Downstream development of the turbulence intensity, $u'/\bar{u}$, for the regular grid RG (⊟) and the fractal grids FG1 (△), FG2 (○), FG3 (◇) and FG4 (✳).

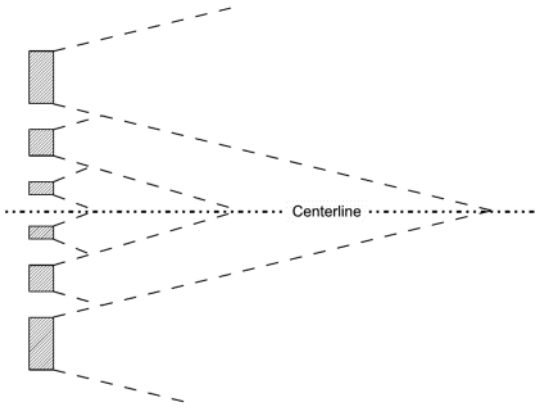

Fig. 5: Wake interaction behind a fractal grid (courtesy of [4]). Reproduced with permission.

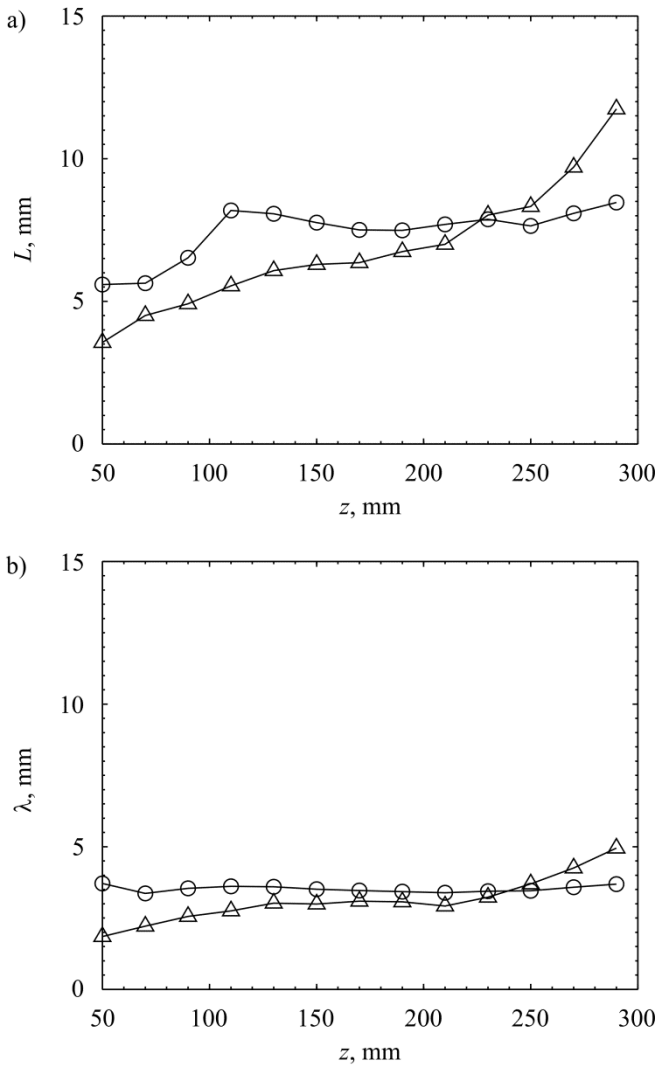

Fig. 6: Downstream development of the integral length scale, L, and the Taylor length scale, λ, for the fractal grid FG2 (-○-) and the regular grid RG (-△-).

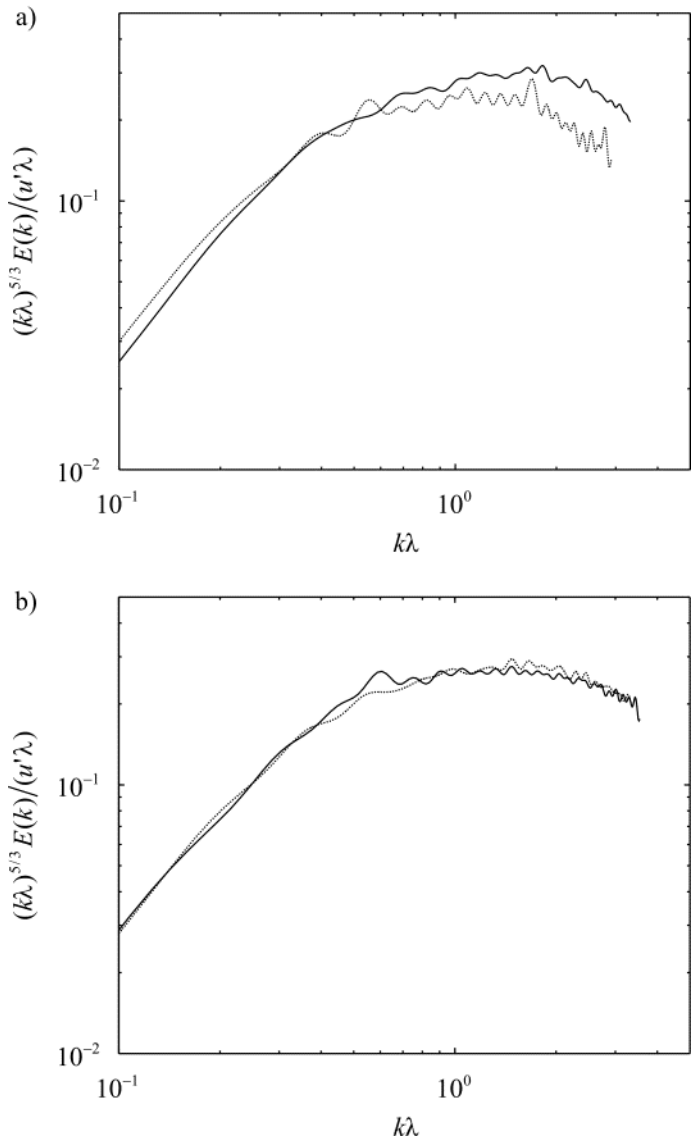

Fig. 7: One-dimensional compensated energy spectra normalised with u' and λ at two different downstream positions (—— 150 mm, ····· 210 mm) for a) the RG and b) the FG2.

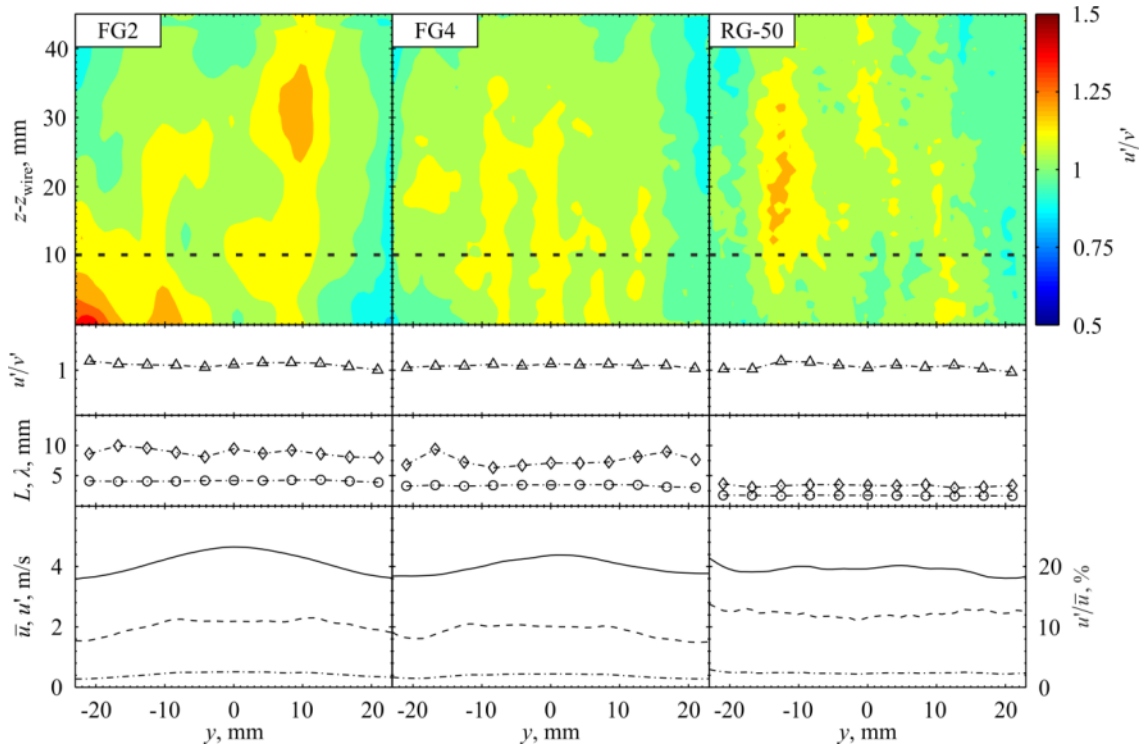

Fig. 8: Assessment of flow isotropy and homogeneity in the region of the flame investigations for the FG2 (three fractal iterations), the FG4 (four fractal iterations) and the RG-50. The field of view started at $z_{wire} = 180$ mm downstream of the grid for the FG2 and FG4 and at $z_{wire} = 50$ mm for the RG-50. The transverse profiles of the isotropy factor, u'/v' (-△-), the integral length scale, L (-◈-), the Taylor length scale, λ (-⊖-), the mean velocity, $\bar{u}$ (——), the root-mean-squared velocity fluctuations, u' (-·-·-), and the turbulence intensity, $u'/\bar{u}$ (- - -), were extracted 10 mm downstream of the flame stabilizing wire, indicated by the dashed line, which was just upstream of the flame brush.

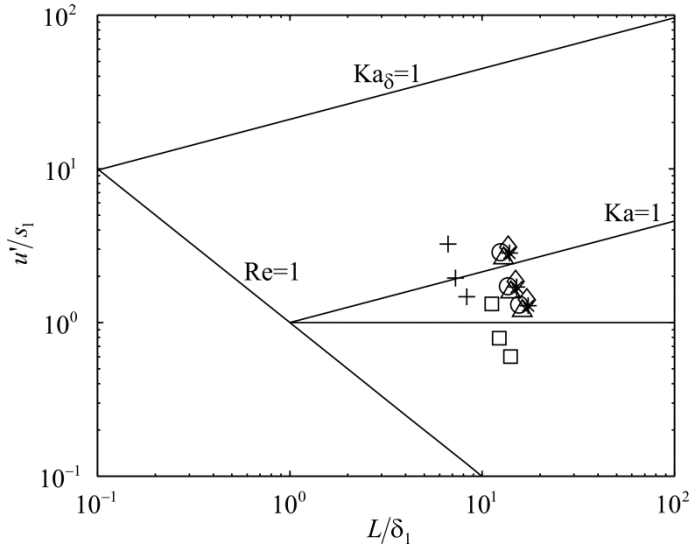

Fig. 9: Regime diagram of the RG-50 (+), RG-180 (□), FG1 (△), FG2 (○), FG3 (◇) and FG4 (✳) flames. The three data points of each grid from top to bottom belong to ϕ = 0.7, 0.8 and 0.9, respectively.

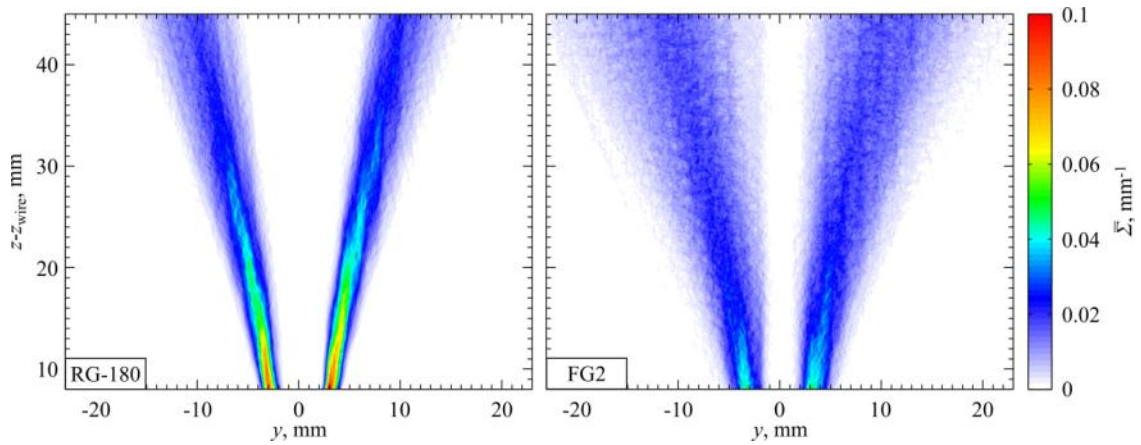

Fig. 10: Two-dimensional FSD distributions of the flames which were stabilized 180 mm downstream of the regular grid RG and the fractal grid FG2.

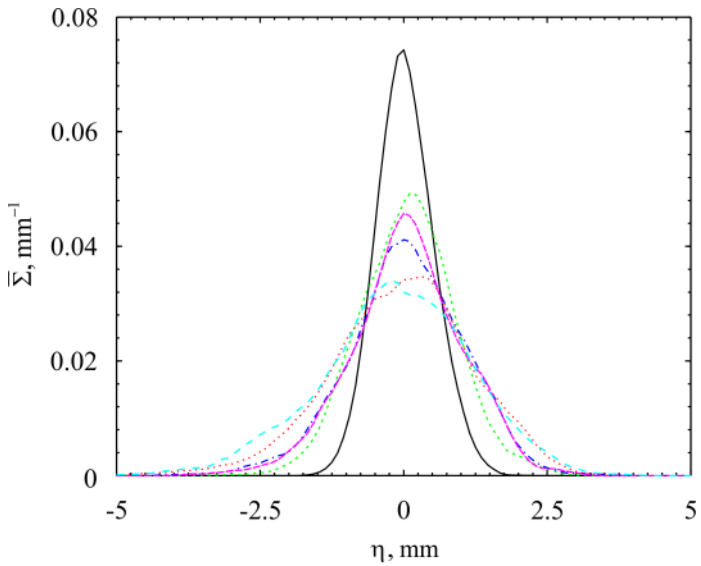

Fig. 11: Transverse profiles of mean FSD for the RG-50 (- - -), RG-180 (——), FG1 (·····), FG2 (-·-·-), FG3 (·····) and FG4 (—·—) flames. The profiles were extracted 10 mm downstream of the flame stabilizing wire, normal to the $\bar{c} = 0.5$ iso-surface to normalize the different flame angles and then shifted along the normal axis, η, in order for the FSD peaks to coincide at the same transverse position.

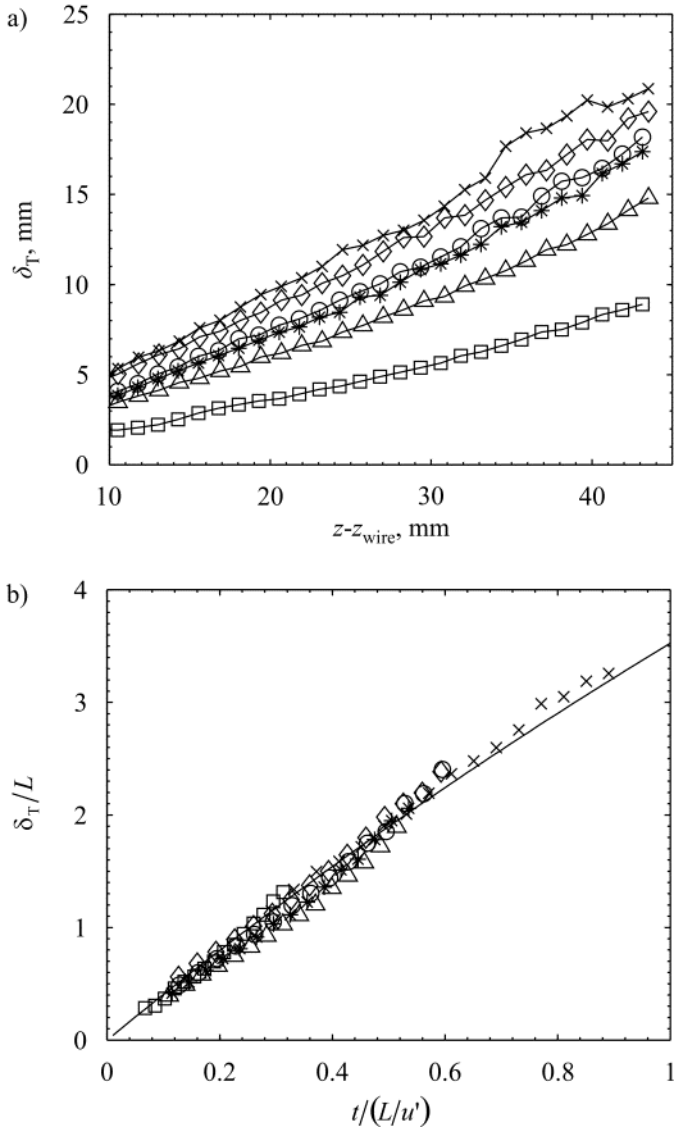

Fig. 12: Downstream development of mean flame brush thickness for the RG-50 (+), RG-180 (□), FG1 (△), FG2 (○), FG3 (◇) and FG4 (✳): a) Brush thickness, δ_T, as a function of downstream distance. b) Dimensionless brush thickness, δ_T/L, as a function of dimensionless time, $t/(L/u')$. The solid line represents Taylor's theory of turbulent diffusivity (Eq. 6).

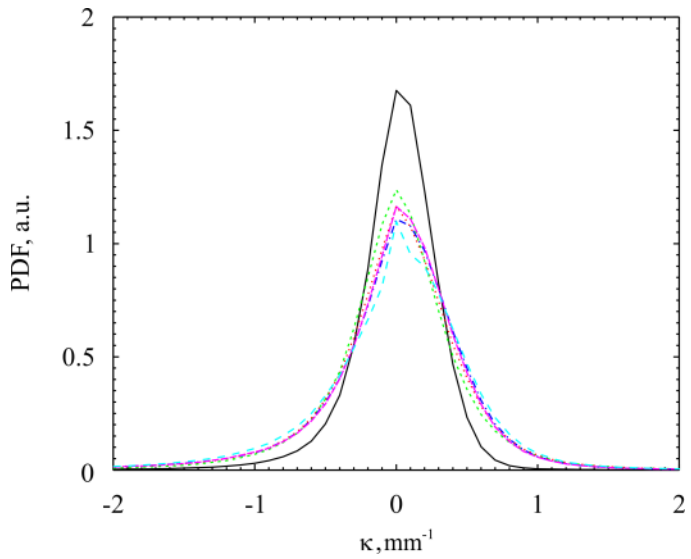

Fig. 13: Probability density functions of flame front curvature, κ, for the RG-50 (- - -), RG-180 (——), FG1 (·····), FG2 (-·-·-), FG3 (·····) and FG4 (-·-·-).

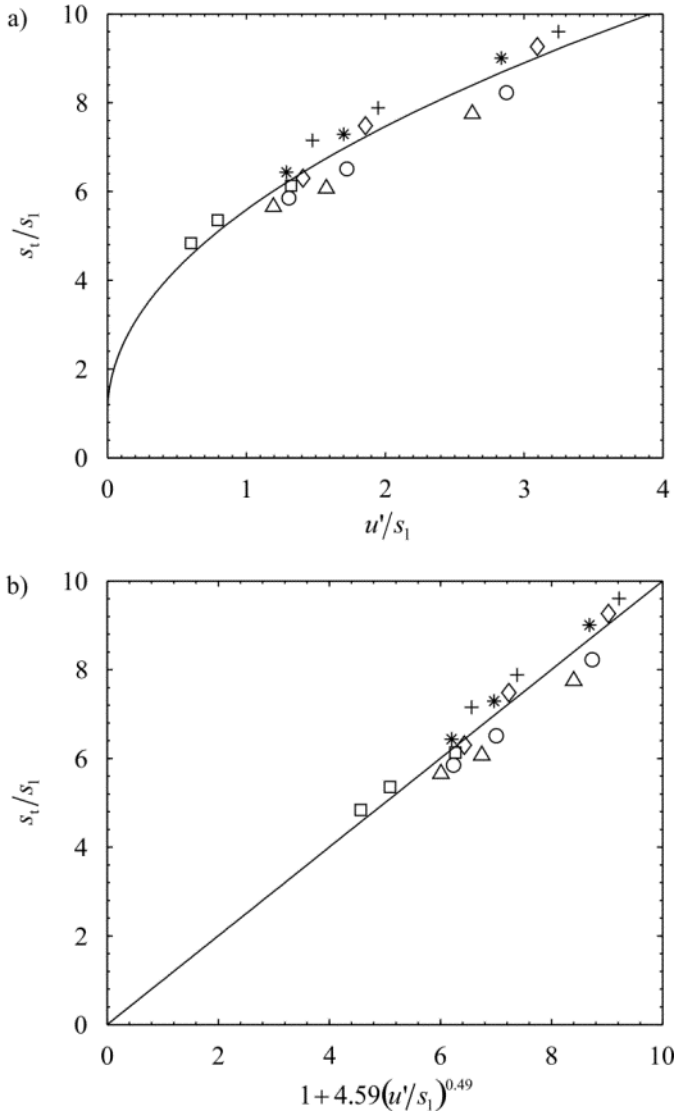

Fig. 14: a) Normalized turbulent burning velocity, s_t/s_l, as a function of the normalized velocity fluctuations of the flow, u'/s_l, for the RG-50 (+), RG-180 (□), FG1 (△), FG2 (○), FG3 (◊) and FG4 (✳). Points from right to left are for $\phi = 0.7$, 0.8 and 0.9, respectively. The solid line shows the best fit of Eq. 8 to the experimental data. b) Normalized turbulent burning velocity as a function of the best fit.

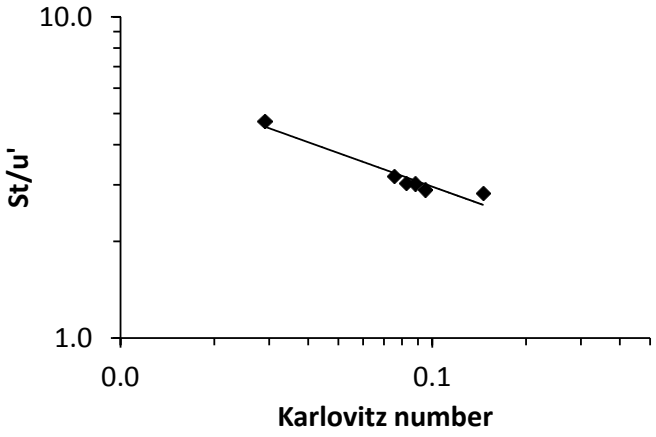

Fig. 15: The dependence of the turbulent burning velocity on the Karlovitz number, for the ϕ = 0.7 flames. The best fit line on the data is $s_t/u' = 1.33\mathrm{Ka}^{-0.348}$.

Tables

Table 1: Relevant design parameters of the investigated grids

	RG	FG1	FG2	FG3	FG4
σ, %	60	35	35	37	35
M, mm	7.75	-	-	-	-
R_d	-	0.56	0.43	0.43	0.43
N	-	3	3	3	4
l_0, mm	-	38.13	38.57	38.88	35.88
d_0, mm	-	3.03	3.84	4.22	3.27
$z^* = l_0^2/d_0$, mm	-	479	387	358	393

Table 2: Parameters used for the flame comparison ($\phi = 0.7$): The laminar burning velocity is $s_l = 0.15$ m/s [48] and the thermal flame front thickness is $\delta_l = 0.68$ mm [49]. The velocity values $\bar{u}$ and u' were taken from the non-reacting PIV data, 10 mm downstream of the wire. The integral length scale L was taken from the centreline hot-wire measurements in non-reacting flow at the same downstream position.

	RG-50	RG-180	FG1	FG2	FG3	FG4
z_{wire}, mm	50	180	180	180	180	180
$\bar{u}$, m/s	3.87	4.04	4.28	4.15	4.14	4.11
u'/s_l	3.25	1.32	2.62	2.87	3.10	2.84
L/δ_l	5.89	9.92	11.34	11.00	12.05	12.22
Re_t	130	89	204	215	254	236